Available online at www.sciencedirect.com
ScienceDirect
Comput. Methods Appl. Mech. Engrg. 392 (2022) 114582
Computer methods in applied mechanics and engineering
www.elsevier.com/locate/cma

Analysis of heterogeneous structures of non-separated scales using curved bridge nodes

Ming Li*, Jingqiao Hu

State Key Laboratory of CAD&CG, Zhejiang University, Hangzhou, China

Received 20 August 2021; received in revised form 14 December 2021; accepted 4 January 2022
Available online xxxx

Abstract

Numerically predicting the performance of heterogeneous structures without scale separation is a challenging task owing to the critical requirements related to computational scalability and efficiency that must be satisfied. In addition, adopting a sufficiently fine mesh to consider the small-scale heterogeneities results in prohibitive computational costs, whereas neglecting them tends to drastically over-stiffen the rigidity of the structure.

Thus, this study proposed an approach for constructing new material-aware shape (basis) functions per element for a coarse discretization of the structure considering each *curved bridge node (CBN)* that is defined along the boundaries of the elements. Rather than formulating their derivation by regarding them as a nonlinear optimization problem, the shape functions were constructed mapping the CBNs to the interior nodes and were subsequently presented in an explicit matrix form as a product of Bézier interpolation and boundary–interior transformations. The CBN shape function captures the heterogeneity of the coarse element with greater flexibility, overcomes the important and challenging issues of inter-element stiffness and displacement discontinuity across interfaces between coarse elements, and improves the analysis accuracy by several orders of magnitude. Moreover, they satisfy the basic geometric properties of shape functions, thereby avoiding non-physical analysis results. Furthermore, the performance of the proposed approach was tested and demonstrated through extensive numerical examples, including a 3D industrial example of billions of degrees of freedom, and comparisons with results obtained from classical approaches were made.

Keywords: Curved bridge nodes (CBNs); Shape functions; Heterogeneous structures; Scale separation; Substructuring; Multiscale analysis

1. Introduction

Heterogeneous structures comprise varied material properties at different locations within their interior structure, and can be found in different types of natural objects, such as human bones and organs [1], or in fabricated objects, such as engineered alloys, polymers, and reinforced composites [2]. The numerical prediction of the physical performance of such heterogeneous structures is a perpetual and fundamental problem in engineering design [3]; moreover, satisfying the critical requirements on computational scalability and efficiency remains a significant challenge when attempting to develop elaborate numerical methods [4–9]. Classical finite element (FE) methods

* Corresponding author.
E-mail address: liming@cad.zju.edu.cn (M. Li).

https://doi.org/10.1016/j.cma.2022.114582
0045-7825/

can capture the behavior of structures (only elasticity is studied here) if a sufficiently fine mesh is adopted to consider the small-scale heterogeneities [10]; however, it results in prohibitive computational costs, particularly when the structures possess highly complex geometries and material distributions. In contrast, neglecting these fine heterogeneities tends to result in the issue of *inter-element stiffness* [11,12], which renders the structure deformation considerably more rigid than in reality.

A possible strategy to address the issue involves the use of parallel computation based on domain decomposition methods (DDM) [13–15]. Another approach involves significantly reducing the scope of the problem using a coarse grid via a geometric multigrid [16] or algebraic multigrid [17,18]. However, these methods are not efficient in the case of structures containing large heterogeneities or high contrast of materials, particularly when the subdomain interface intersects the heterogeneities. Further details can be found in [19–21].

The application of multiscale methods to predict the behavior of heterogeneous structures is on the rise. Typically, the analysis is achieved via two levels of FE simulations – macroscale and microscale – wherein the analysis results on each microstructure are used in parallel to aid in the prediction of the overall performance of the structure in the macroscale, and vice versa. Numerical Homogenization is a typical mean-field multiscale analysis approach that replaces each microstructure with an effective elasticity tensor using the calculation results obtained from the microstructure analysis via the asymptotic [22–24] and energy-based approaches [25,26]. The heterogeneous coarse mesh element is replaced as an averaged homogenized material under a set of classical mechanical tests: stretching horizontally and vertically, and shearing. The multi-level FE method (FE^2) is another important multiscale approach, wherein the FE analysis is conducted iteratively via transiting between fields (stress and strain) in the macroscale and microscale until convergence [27–29]. The FE^2 approach can capture microscopic heterogeneous information with greater accuracy, although the computational costs are considerable. Both approaches of numerical Homogenization and FE^2 usually assume scale separation, that is, the length scale of the microstructure is much lower than that of the structural length scale. However, this assumption is not valid when considering the analysis of heterogeneous structures without scale separation, which is the focus of this study. Consequently, researchers have developed various approaches to address this issue, including the high-order computational Homogenization [30–32], fiber-based Homogenization [33], and direct FE^2 [34]. A comprehensive literature review on FE^2 can be found in [35], and that on multiscale in [3].

Substructuring is another aspect that is studied for the analysis of heterogeneous structures [36,37], wherein all the structures are considered a set of substructures connected by boundary nodes between the coarse elements that are referred to as *super-elements*. Thereafter, according to a local FE formulation of each coarse element, a matrix condensation strategy ultimately produces a linear equation regarding the super-elements, whose solution consequently yields the global solution in the fine mesh. Although Substructuring yields a high-accuracy solution, it faces two primary challenges that prohibit its industrial applications. First, the local analysis problem per coarse mesh element involves solution computations to excessive numbers of linear equation systems, which increases costs. Moreover, in contrast to the fine-scale analysis problem, it produces a dense global stiffness matrix with more non-zero elements; an example is shown in Fig. 10. In addition, the Substructuring approach is only applicable to linear problems.

Constructing tailored material-aware shape (or “basis”) functions has shown great potential in terms of analysis of heterogeneous structures of non-separated scales, and is also referred to as the multiscale FE method [38,39]. These approaches substitute classical FE shape functions per coarse mesh element with newly constructed complex ones that have been obtained by performing fine scale calculations. Moreover, these approaches overcome two primary challenges: closely capturing the heterogeneity of the coarse element and maintaining the global solution continuity in the fine mesh. Most previous studies have focused on the first challenge, and have articulated the shape function construction as a spectral expansion [38,39] or constrained nonlinear optimization problem [12,21]. More recently, Le et al. developed a novel Coarse Mesh Condensation Multiscale Method (CMCM) approach for a better solution approximation via second-order strain fields [21]. Although the previous approaches could partially overcome the inter-element stiffness caused by the use of linear shape functions in conventional FE methods, generally, the produced shape functions cannot satisfy the basic property of partition of unity (PU), thereby resulting in deformations of non-physical behaviors. To resolve the issue, a set of discontinuous and matrix-valued shape functions were derived by Chen [12], where the basic geometric properties of shape functions were imposed as constraints in an optimization problem. However, these studies have been unable to completely address the issue of the global solution continuity. Further discussion on the previous approaches is presented in Section 5.

Table 1
Summary of important notations in this paper.

Ω^α	:	Coarse element
ω_e^α	:	Fine element, simplified as ω_e
$\mathcal{M}^H$	:	Coarse mesh, set of discrete coarse elements in the whole domain
$\mathcal{M}^h$	:	Global fine mesh, set of discrete fine elements in the whole domain
$\mathcal{M}^{\alpha,h}$	:	Local fine mesh, set of discrete fine elements in Ω^α
M	:	Number of coarse elements of $\mathcal{M}^H$
m	:	Number of fine elements of $\mathcal{M}^{\alpha,h}$
$\mathcal{X}_c$	:	Corner nodes of local fine mesh $\mathcal{M}^{\alpha,h}$
$\mathcal{X}_b$	:	Boundary nodes of local fine mesh $\mathcal{M}^{\alpha,h}$
$\mathcal{X}_i$	:	Interior nodes of local fine mesh $\mathcal{M}^{\alpha,h}$
$\mathcal{X}_r$	:	Bridge nodes as subset of $\mathcal{X}_b$ of local fine mesh $\mathcal{M}^{\alpha,h}$
$\mathbf{Q}$	:	Vector of displacements of all CBNs of $\mathcal{M}^H$
$\mathbf{Q}^\alpha$	:	Vector of displacements of all CBNs of Ω^α
$\mathbf{q}_s$	:	Vector of displacements of nodes in $\mathcal{X}_s$, where s could be b, i
$\mathbf{q}$	:	Vector of displacements of nodes in $\mathcal{M}^{\alpha,h}$, including $\mathbf{q}_i$ and $\mathbf{q}_b$
$\mathbf{K}^\alpha$	:	Stiffness matrix of a coarse element Ω^α
$\mathbf{k}^\alpha$	:	Stiffness matrix of a local fine mesh $\mathcal{M}^{\alpha,h}$
$\boldsymbol{\Psi}$	:	The Bézier interpolation matrix relating $\mathbf{Q}^\alpha$ to $\mathbf{q}_b$
$\mathbf{M}^\alpha$	:	The boundary–interior transformation matrix relating $\mathbf{q}_b$ to $\mathbf{q}_i$
$\mathbf{N}_e(\mathbf{x})$	:	The basic bilinear shape function on point $\mathbf{x}$ of a fine element ω_e
$\mathbf{N}^h(\mathbf{x})$	:	Assembly of all $\mathbf{N}_e(\mathbf{x})$ in local fine mesh $\mathcal{M}^{\alpha,h}$
$\mathbf{N}^\alpha(\mathbf{x})$	:	The CBN shape functions of a coarse element Ω^α
$\mathbf{I}_{d,1}$	:	An all-one vector with size of $d \times 1$
$\mathbf{I}_d$	:	An identity matrix with size of $d \times d$

In this study, to realize the linear elasticity analysis of heterogeneous structures of non-separated scales, an approach that introduces a new concept of *curved bridge nodes (CBNs)*, induced from a subset of the boundary nodes, is proposed. In addition, suitable extensions of the CBN-based analysis to nonlinear elastic problems (of the neo-Hookean model) were discussed. In contrast to previous approaches that focused on corner nodes, the CBN analysis approach can accommodate more DOFs in analysis via the construction of a parametric cubic Bézier curve or surface [40] along the interfaces between the coarse elements. Consequently, it generates an *explicit* set of new CBN shape functions, which overcome the challenging issue of inter-element stiffness and ensure the global solution continuity in the fine mesh scale. Moreover, the basic geometric properties of shape functions are also satisfied, thereby avoiding non-physical analysis results. Furthermore, the analysis accuracy and efficiency of the proposed approach is tested using various numerical examples, including a 3D industrial example of billions of DOFs, and compared with certain classical approaches.

2. Problem statement and approach overview

To provide a clear explanation, a 2D linear elastic body is mainly used to describe the approach for analysis. Its extensions to a 3D case and to nonlinear models are described later in Section 4. Important notations are also summarized in Table 1).

2.1. Linear elasticity analysis of heterogeneous structures

As illustrated in Fig. 1(a), let $\Omega \subset \mathbb{R}^d$ for dimension $d = 2$ be a heterogeneous solid structure under study, which may comprise different elasticity tensors $\mathbf{D}(\mathbf{x})$ at different locations $\mathbf{x} \in \Omega$. The linear elasticity analysis of Ω is described by a displacement vector for each point $\mathbf{x}$ as $\mathbf{u}(\mathbf{x}) = (u(\mathbf{x}), v(\mathbf{x}))^T$. Further, the *strain vector* $\boldsymbol{\varepsilon}(\mathbf{x}, \mathbf{u})$ is defined as a linear approximation to the Green's strain, and is represented in vector form as

$$\boldsymbol{\varepsilon}(\mathbf{x}, \mathbf{u}) = (\boldsymbol{\varepsilon}_{11}, \boldsymbol{\varepsilon}_{22}, \sqrt{2}\boldsymbol{\varepsilon}_{12})^T, \tag{1}$$

and the *stress vector* $\boldsymbol{\sigma}(\mathbf{u})$ is defined via Hooke's law,

$$\boldsymbol{\sigma}(\mathbf{x}) = (\boldsymbol{\sigma}_{11}, \boldsymbol{\sigma}_{22}, \sqrt{2}\boldsymbol{\sigma}_{12})^T = \mathbf{D}(\mathbf{x})\ \boldsymbol{\varepsilon}(\mathbf{u}). \tag{2}$$

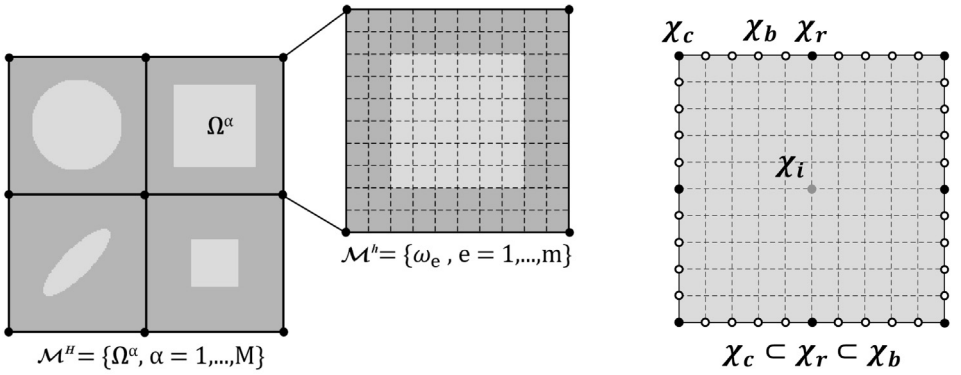

(a) Structure and its coarse and fine elements (b) Node types

Fig. 1. (a). Structure Ω, coarse mesh $\mathcal{M}^H = \{\Omega^\alpha\}$, local fine mesh $\mathcal{M}^{\alpha,h} = \{\omega_e^\alpha,\ e = 1, 2, \ldots, m\}$. (b). Fine mesh nodes are classified into three classes: corner nodes $\mathcal{X}_c$, boundary nodes $\mathcal{X}_b$, and bridge nodes $\mathcal{X}_i$, where $\mathcal{X}_c \subseteq \mathcal{X}_r \subseteq \mathcal{X}_b$.

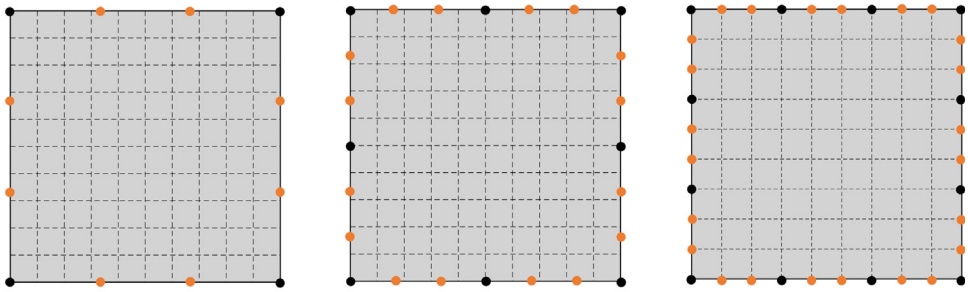

(a) Corner nodes as bridge nodes. (b) Add 1 bridge node each edge. (c) CBN equal boundary nodes

Fig. 2. Curved bridge nodes (CBNs in orange) introduce additional nodes between adjacent bridge nodes (in black), and are considered as analysis DOFs in the proposed CBN heterogeneous structure analysis approach. The CBNs may or may not be coincident boundary nodes depending on the settings of fine mesh size or bridge nodes. (For interpretation of the references to color in this figure legend, the reader is referred to the web version of this article.)

The linear elasticity analysis of Ω aims to determine the displacement $\mathbf{u}$ that satisfies

$$\begin{cases} -\text{div}\boldsymbol{\sigma}(\mathbf{u}(\mathbf{x})) = \mathbf{g}, & \text{in } \Omega, \\ \boldsymbol{\sigma}(\mathbf{u}(\mathbf{x})) \cdot \mathbf{n} = \boldsymbol{\tau}, & \text{on } \Gamma_N, \\ \mathbf{u}(\mathbf{x}) = \mathbf{u}_0, & \text{on } \Gamma_D, \end{cases} \tag{3}$$

where Γ_D is a fixed boundary of a prescribed displacement $\mathbf{u}_0$, Γ_N is the loading boundary of an external loading $\boldsymbol{\tau}$, and $\mathbf{g}$ is the body force.

The differential form in Eq. (3) can also be stated as a weak form to induce its FE analysis. Thus, the displacement $\mathbf{u} \in H^1(\Omega)$ satisfies

$$a(\mathbf{u}, \mathbf{v}) = l(\mathbf{v}), \quad \forall\ \mathbf{v} \in H_0^1(\Omega), \tag{4}$$

where

$$a(\mathbf{u}, \mathbf{v}) = \int_\Omega \boldsymbol{\sigma}(\mathbf{u}) \cdot \boldsymbol{\varepsilon}(\mathbf{v})\ \text{dV} = \int_\Omega \boldsymbol{\varepsilon}(\mathbf{u})^T\ \mathbf{D}(\mathbf{x})\ \boldsymbol{\varepsilon}(\mathbf{v})\ \text{dV}, \tag{5}$$

and

$$l(\mathbf{v}) = \int_\Omega \mathbf{g} \cdot \mathbf{v}\ \text{dV} + \int_{\Gamma_N} \boldsymbol{\tau} \cdot \mathbf{v}\ dS, \tag{6}$$

where $H^1(\Omega)$ and $H_0^1(\Omega)$ are the usual Sobolev vector spaces, and $\mathbf{v}$ represents the test vector function.

2.2. Preliminary: bridge nodes and shape functions

The FE analysis of the linear elasticity problem in Eq. (3) or (4) is typically conducted on a discretized domain of Ω. Two different meshes were considered in this study, as indicated in Fig. 1(a). The *coarse mesh* $\mathcal{M}^H = \{\Omega^\alpha,\ \alpha = 1, 2, \ldots, M\}$ contains a set of disjoint discrete *heterogeneous coarse elements* Ω^α of large size. Each coarse element Ω^α further consists of a *local fine mesh* $\mathcal{M}^{\alpha,h} = \{\omega_e^\alpha,\ e = 1, 2, \ldots, m\}$, composed of disjoint *homogeneous fine elements* ω_e^α of much smaller size, which together induce the *global fine mesh* $\mathcal{M}^h = \{\omega_e^\alpha,\ e = 1, 2, \ldots, m,\ \alpha = 1, 2, \ldots, M\}$.

Further, each FE is formed by a set of nodes. For a particular local fine mesh $\mathcal{M}^{\alpha,h}$ and a coarse element Ω^α, their corresponding nodes can be classified into three different subsets depending on their locations: sets of *corner nodes, boundary nodes, or interior nodes*, denoted as $\mathcal{X}_c,\ \mathcal{X}_b,\ \mathcal{X}_i$, respectively. This is shown in Fig. 1(b).

Herein, the concept of *bridge node* set as a subset of the boundary node set is introduced, which is denoted as $\mathcal{X}_r$ and defined as follows

$$\mathcal{X}_c \subseteq \mathcal{X}_r \subseteq \mathcal{X}_b. \tag{7}$$

For a particular segment determined by a pair of adjacent bridge nodes in $\mathcal{X}_r$, a set of equally spaced nodes are inserted, which, coupled with the bridge nodes themselves, form the set of *CBNs*. As explained in Section 3.1, these nodes aid in the downstream task in high-order interpolation curve construction. Although the bridge nodes may acquire the corner nodes, or a subset of the boundary nodes, the CBNs do not have to be coincident with the boundary nodes. For example, as shown in Fig. 2 , different relationships between bridge nodes and CBNs can be observed under different fine mesh size settings of 10×10 to 9×9 in (c), or choices of bridge nodes.

Shape functions act as the basis functions in FE analysis, whose linear combinations are used to describe a deformation of structure under study. First the definition on the local fine mesh $\mathcal{M}^{\alpha,h}$ must be understood. For a particular master FE ω_e with four corner nodes within the range $(x, y) \in [-1, 1] \times [-1, 1]$ and numbered from 1 to 4, the scalar *bilinear shape function* $N_i(\mathbf{x})$ is defined as

$$N_i(\mathbf{x}) : \Omega \to \mathbb{R}, \quad N_i(\mathbf{x}) = \frac{1}{4}(1 + x_i x)(1 + y_i y) \quad , i = 1, 2, 3, 4. \tag{8}$$

Accordingly, the solution $\mathbf{u}(\mathbf{x})$ to problem (3), (4), is interpreted as a linear combination of the shape functions, or in a matrix form, as follows:

$$\mathbf{u}_e(\mathbf{x}) = \mathbf{N}_e(\mathbf{x})\ \mathbf{q}_e, \quad \mathbf{x} \in \omega_e, \tag{9}$$

where $\mathbf{q}_e$ is the displacement vector of dimension 8×1, and $\mathbf{N}_e(\mathbf{x})$ is the matrix form of $N_i(\mathbf{x})$ of dimension 2×8,

$$\mathbf{N}_e(\mathbf{x}) = \begin{bmatrix} N_1(\mathbf{x}) & 0 & N_2(\mathbf{x}) & 0 & N_3(\mathbf{x}) & 0 & N_4(\mathbf{x}) & 0 \\ 0 & N_1(\mathbf{x}) & 0 & N_2(\mathbf{x}) & 0 & N_3(\mathbf{x}) & 0 & N_4(\mathbf{x}) \end{bmatrix}. \tag{10}$$

Consequently, the *partition of unity (PU)* and *Lagrange property* are satisfied for $N_i(\mathbf{x}),\ i = 1, 2, 3, 4$, that is,

$$\mathbf{N}_e(\mathbf{x})\ \mathbf{I}_{8,1} = \mathbf{I}_{2,1}, \quad \text{and} \quad N_i(\mathbf{x}_j) = \delta_{ij}, \tag{11}$$

where $\mathbf{I}_{d,1}$ is an all-one vector with size $d \times 1$, and δ_{ij} is the Kronecker delta function.

In addition, the property of *node interpolation* directly originates from the Lagrange property as

$$\mathbf{N}_e(\mathbf{x}_j)\ \mathbf{q}_e = \mathbf{q}_{e,j}, \tag{12}$$

where $\mathbf{q}_{e,j}$ is the displacement of $\mathbf{q}_e$ on a node $\mathbf{x}_j$.

The bilinear shape functions derived above can be defined on the global fine $\mathcal{M}^h$ or coarse $\mathcal{M}^H$ meshes. Regarding $\mathcal{M}^h$, the shape functions can be defined on a homogeneous fine element ω_e^α, and serve as a basis for the fine displacements, thereby effectively approximating the target solution. However, its numerous fine elements result in high computational costs. In contrast, on coarse mesh $\mathcal{M}^H$, the shape functions are defined on a heterogeneous coarse element Ω^α, which results in a considerable loss in solution accuracy. Thus, this study aimed to resolve these issues via the construction of a set of material-aware shape functions for the CBNs, as discussed in the following sections.

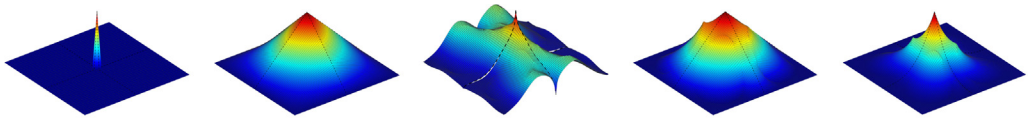

(a) Bilinear shape functions on $\mathcal{M}^h$ (b) Bilinear shape functions on $\mathcal{M}^H$ (c) Shape functions without continuity consideration (d) Shape functions with linear interpolation on interface (e) Shape functions on CBNs with curved interpolation

Fig. 3. Shape functions under different construction strategies.

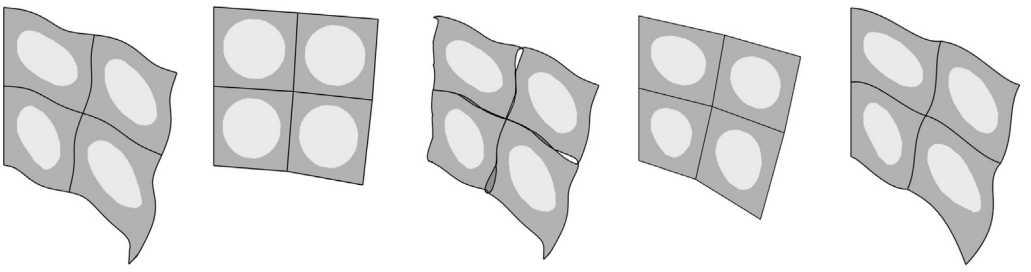

(a) On $\mathcal{M}^h$ (b) On $\mathcal{M}^H$ (c) Without continuity consideration (d) With linear interpolation on interface (e) On CBNs with curved interpolation

Fig. 4. Analysis results using the different shape functions defined in Fig. 3.

2.3. Approach overview

Following the classical Galerkin FE method [41], shape functions act as bases to produce the overall displacement with respect to a vector of discrete nodal values. However, rather than choosing the corner nodes, the CBNs were introduced here and set as the coarse nodes for increased analysis DOFs and improved flexibilities of shape descriptions.

In this study, a set of material-aware CBN shape functions $\mathbf{N}^\alpha(\mathbf{x})$ was constructed for each coarse element Ω^α. Let $\mathbf{Q}$ be the vector of discrete displacements on CBNs in $\mathcal{M}^H$ to be determined, and $\mathbf{Q}^\alpha$ be its component on Ω^α. Accordingly, the displacement on Eq. (3) can be obtained as

$$\mathbf{u}(\mathbf{x}) = \sum_{\alpha=1}^{M} \mathbf{N}^\alpha(\mathbf{x})\ \mathbf{Q}^\alpha. \tag{13}$$

To improve the ability of describing the heterogeneity of fine mesh, the CBN shape function $\mathbf{N}^\alpha(\mathbf{x})$ was constructed as a piecewise-bilinear function (in 2D) defined over the local fine mesh $\mathcal{M}^{\alpha,h}(\mathbf{x})$,

$$\mathbf{N}^\alpha(\mathbf{x}) = \mathbf{N}^h(\mathbf{x})\ \tilde{\boldsymbol{\Phi}}, \tag{14}$$

where $\tilde{\boldsymbol{\Phi}}$ is a matrix of DOFs to be determined for the purpose of closely capturing the heterogeneity of the coarse element, and $\mathbf{N}^h(\mathbf{x})$ is a matrix of the fine-mesh shape functions $\mathbf{N}_e(\mathbf{x})$ in $\mathcal{M}^{\alpha,h}$:

$$\mathbf{N}^h(\mathbf{x}) = \sum_{e=1}^{m} \mathbf{N}_e(\mathbf{x}), \quad \mathbf{x} \in \Omega^\alpha, \tag{15}$$

where $\sum$ denotes the *assembly sum* within the numerical FE assembly process that conducts the summation on the same location. Subsequently, for a specific point $\mathbf{x}_0$, the value of $\mathbf{N}^h(\mathbf{x}_0)$ can be directly evaluated.

However, the construction of effective shape functions is hindered by at least two known challenges: the displacement discontinuity across the coarse element interface and the inter-element stiffness [11,12]. The interface discontinuity issue originates from the fact that the shape functions are usually constructed locally without considering the adjacency of the coarse elements, and thus, they may acquire different values along the common interface [12]. Meanwhile, the inter-element stiffness issue originates from the use of linear interpolation when reconstructing the global fine-mesh displacements from the discrete coarse nodal displacements [11,12], and thus, the boundary tends to be stiffer than it actually deforms in fine scale.

Consider, for example, the results in Figs. 3 and 4, where different shape functions, acquiring different values $\tilde{\boldsymbol{\Phi}}$, are respectively generated for comparison. The shape functions and the direct FE analysis results obtained using the fine $\mathcal{M}^h$ or coarse $\mathcal{M}^H$ meshes are shown in Figs. 3(a),(b) and Fig. 4(a),(b) as benchmarks. Three differently constructed shape functions are further generated, and the results are shown in Fig. 3(c),(d),(e). Consequently, they yield contrasting analysis results, as shown in Fig. 4(c),(d),(e). As evident, the construction without continuity consideration causes interface overlap and discontinuity in Fig. 4(c). In addition, the inter-element stiffness is observed in Fig. 4(d) as well, which results in stiffer deformation than the benchmark in the fine-scale, as in Fig. 4(a).

In an effort to further address the above-mentioned challenges, this study aimed to develop a new class of material-aware shape functions, referred to as CBN shape functions. For a particular master coarse element, this was achieved by considering the shape function construction as a process for mapping the coarse DOFs (or displacements on CBNs) to the local fine displacements per coarse element, rather than formulating it as a constrained nonlinear optimization problem.

First, the cubic Bézier interpolation curves were constructed using the CBNs along the coarse element's boundaries, which ensured the continuity of the global displacement in fine mesh and also improved its accuracy by allowing for greater deformation flexibilities. Second, the boundary nodal displacements were mapped to those on the interior nodes, thereby building on the intrinsic physical properties and closely capturing the heterogeneities of the coarse element. Finally, the shape functions were derived in an explicit matrix form as a product of two matrix transformations: the Bézier interpolation and the boundary–interior transformations, while the basic geometric properties of shape functions were preserved.

In summary, the derived shape functions present the following properties.

1. Defined with respect to CBNs with flexible analysis DOFs, thereby overcoming inter-element stiffness while maintaining the global displacement smoothness.
2. Expressed in an explicit matrix form as a product of two transformations: Bézier interpolation and the boundary–interior transformations, thus avoiding complex nonlinear optimization costs.
3. Preserving the basic geometric properties of shape functions: node interpolation, translation and rotation invariance, and thus avoiding non-physical analysis behaviors.
4. Applicable to nonlinear analysis problems, although at the cost of certain accuracy loss.

3. Construction of CBN shape functions

Considering Fig. 1, let Ω^α be a master coarse element, $\mathcal{M}^{\alpha,h}$ its local fine mesh, and $\mathcal{X}_r$ the given bridge node set. Further, as mentioned, the CBN shape functions $\mathbf{N}^\alpha(\mathbf{x})$ are achieved as a product of two matrix transformations: the Bézier interpolation transformation and the boundary–interior transformation.

3.1. Construction of Bézier interpolation transformation

The Bézier interpolation transformation constructs a map from the discrete displacements on the CBNs $\mathbf{Q}^\alpha$ to those on the boundary nodes in $\mathcal{X}_b$. The higher-order interpolation of the Bézier curve facilitates greater control flexibility while maintaining favorable geometric properties of PU and translation/rotation invariance. Fig. 5 illustrates the difference between different interpolation strategies.

A cubic Bézier curve $\mathbf{P}(t)$ is considered here in the following form [40],

$$\mathbf{P}(t) = \sum_{i=0}^{3} \psi_i(t)\, \mathbf{P}_i, \quad \text{for} \quad \psi_i(t) = C_n^i t^i (1-t)^{3-i}, \tag{16}$$

where $\psi_i(t)$ is a cubic Bernstein basis, $\mathbf{P}_i \in \mathbb{R}^2$ is the control point, and C_n^i is the binomial coefficient.

Further, $\mathbf{P}_i$ are the values of $P(t)$ at node $t = i/3$ for $i = 0, 1, 2, 3$, or,

$$\mathbf{P}(0) = \mathbf{P}_0, \quad \mathbf{P}(1/3) = \mathbf{P}_1, \quad \mathbf{P}(2/3) = \mathbf{P}_2, \quad \mathbf{P}(1) = \mathbf{P}_3. \tag{17}$$

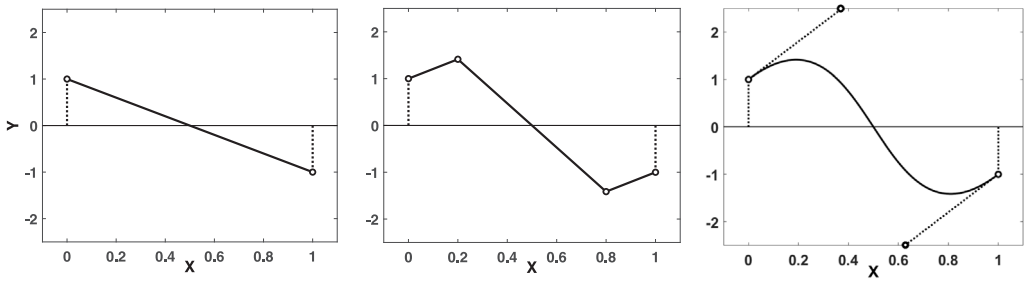

(a) Linear interpolation (b) Linear interpolation with additional nodes (c) Bézier interpolation with additional nodes

Fig. 5. Different interpolation strategies produce different boundary curves, where the higher order cubic Bézier curves exhibit greater flexibility.

In addition, $\mathbf{P}(t)$ exhibits the properties of the translation and rotation invariance for a constant angular velocity $\hat{\theta}$ of dimension 2×2,

$$\sum_{i=0}^{3} \psi_i(t) = 1, \quad \hat{\theta} \times \mathbf{P}(t) = \sum_{i=0}^{3} \psi_i(t)\, \hat{\theta} \times \mathbf{P}_i, \tag{18}$$

regarding the cross product $\times$, which were used in delivering such properties of the CBN shape functions.

Now, consider the approach for constructing the Bézier transformation matrix. Following the idea of FE displacement expression in Eq. (9), $\mathbf{P}(t)$ can be rewritten in the following matrix form,

$$\underset{(2\times 1)}{\mathbf{P}(t)} = \underset{(2\times 8)}{\boldsymbol{\psi}(t)} \; \underset{(8\times 1)}{\mathbf{P}}, \tag{19}$$

for

$$\mathbf{P} = [\mathbf{P}_0, \mathbf{P}_1, \mathbf{P}_2, \mathbf{P}_3]^T, \tag{20}$$

and

$$\boldsymbol{\psi}(t) = \boldsymbol{\psi}_0(t) \otimes \mathbf{I}_2 = \begin{bmatrix} 1 & t & t^2 & t^3 \end{bmatrix} \begin{bmatrix} 1 & 0 & 0 & 0 \\ -3 & 3 & 0 & 0 \\ 3 & -6 & 3 & 0 \\ -1 & 3 & -3 & 1 \end{bmatrix} \otimes \mathbf{I}_2 \tag{21}$$

$$= \begin{bmatrix} \psi_0(t) & 0 & \psi_1(t) & 0 & \psi_2(t) & 0 & \psi_3(t) & 0 \\ 0 & \psi_0(t) & 0 & \psi_1(t) & 0 & \psi_2(t) & 0 & \psi_3(t) \end{bmatrix},$$

where the Kronecker product $\otimes$ with identity matrix $\mathbf{I}_2$ (with size of 2×2) is used to match the dimensions of the column vector $\mathbf{P}$.

Suppose E is a line segment bounded by a pair of adjacent bridge nodes in $\mathcal{X}_r$, and $t(\cdot)$ is a function that re-parameterizes E into a parametric curve in a range of $[0, 1]$. Then, by inserting two additional equally spaced nodes along E, or at $t = 1/3, 2/3$, in total, the four associated CBNs can be obtained.

Let $\mathbf{Q}_E$ be the vector of the x, y displacements at the four CBNs. Considering $\mathbf{Q}_E$ as the control point in the cubic Bézeir curve function (19), the interpolation displacement function $\mathbf{u}_E(\mathbf{x})$ along segment E is obtained as

$$\underset{(2\times 1)}{\mathbf{u}_E(\mathbf{x})} = \underset{(2\times 8)}{\boldsymbol{\psi}_E(t(\mathbf{x}))} \; \underset{(8\times 1)}{\mathbf{Q}_E}, \tag{22}$$

where $\boldsymbol{\psi}_E(t(\mathbf{x}))$ is in a form as Eq. (21).

From Eq. (17), it is evident that evaluating $\mathbf{u}_E(\mathbf{x})$ at the four CBNs in E provides the four control points $\mathbf{Q}_E$. Consequently, the relation can be derived on the full boundary nodes in $\mathcal{X}_b$.

Consider a specific boundary node $\mathbf{x}_0$ in $\mathcal{X}_b$ located at segment E. Evaluating $\boldsymbol{\psi}_E(t(\mathbf{x}))$ at $\mathbf{x}_0$ provides the corresponding interpolated displacement $\boldsymbol{\psi}_E(t(\mathbf{x}_0))$. Thus, following a similar FE assembly process, the interpolation matrix of $\mathbf{x}_0$ can be obtained

$$\underset{(2\times 6r)}{\bar{\boldsymbol{\psi}}(\mathbf{x}_0)} = \sum_{E} \boldsymbol{\psi}_E(t(\mathbf{x}_0)), \quad \mathbf{x}_0 \in E. \tag{23}$$

Thereafter, iterating $\mathbf{x}_0$ for all the boundary nodes in $\mathcal{X}_b$, the following is obtained

$$\underset{(2b\times 1)}{\mathbf{q}_b} = \underset{(2b\times 6r)}{\boldsymbol{\Psi}} \; \underset{(6r\times 1)}{\mathbf{Q}^\alpha}, \tag{24}$$

where the *Bézier interpolation matrix* is

$$\underset{(2b\times 6r)}{\boldsymbol{\Psi}} = \left[\bar{\boldsymbol{\psi}}(\mathbf{x}_0),\ \mathbf{x}_0 \in \mathcal{X}_b\right], \tag{25}$$

and subsequently, their corresponding bases $\bar{\boldsymbol{\psi}}(\mathbf{x}_0)$ are listed individually in terms of rows, with $\mathbf{Q}^\alpha$ being the vector of all displacements on CBNs of Ω^α.

The dimension $6r$ of $\mathbf{Q}^\alpha$ is evident owing to the r line segments from the r bridge nodes, which together possess $3r$ CBNs, and are thus of a dimension $6r$ considering its x-, y-components.

3.2. Construction of boundary–interior transformation

For the vector $\mathbf{q}_b$ of the boundary displacements in Eq. (24), a boundary–interior transformation was constructed to map it to the interior displacements. Let $\mathbf{k}^\alpha$ be the associated stiffness matrix on the local fine mesh $\mathcal{M}^{\alpha,h}$. Consequently, all DOFs were reordered to partition them into internal and boundary entries indexed by i and b, denoted as vectors $\mathbf{q}_i, \mathbf{q}_b$. Their relation is determined by the following FE equilibrium equation

$$\begin{bmatrix} \mathbf{k}_b & \mathbf{k}_{bi} \\ \mathbf{k}_{ib} & \mathbf{k}_i \end{bmatrix} \begin{bmatrix} \mathbf{q}_b \\ \mathbf{q}_i \end{bmatrix} = \begin{bmatrix} \mathbf{f}_b \\ 0 \end{bmatrix}, \tag{26}$$

where $\mathbf{k}_b,\ \mathbf{k}_i,\ \mathbf{k}_{bi},\ \mathbf{k}_{ib}$ are the associated stiffness sub-matrices of $\mathbf{k}^\alpha$, and $\mathbf{f}_b$ is a vector of exposed forces on the boundary nodes.

Considering the second-row

$$\underset{(2i\times 1)}{\mathbf{q}_i} = \underset{(2i\times 2b)}{\mathbf{M}^\alpha} \; \underset{(2b\times 1)}{\mathbf{q}_b}, \quad \text{for} \quad \underset{(2i\times 2b)}{\mathbf{M}^\alpha} = -\underset{(2i\times 2i)}{\mathbf{k}_i^{-1}} \; \underset{(2i\times 2b)}{\mathbf{k}_{ib}}. \tag{27}$$

Accordingly, the vector of the displacements on $\mathcal{M}^{\alpha,h}$ is obtained as

$$\underset{(2i+2b)\times 1}{\mathbf{q}} = [\mathbf{q}_b, \mathbf{q}_i]^T = \underset{(2i+2b)\times 2b}{\tilde{\mathbf{M}}^\alpha} \; \mathbf{q}_b, \tag{28}$$

where $\tilde{\mathbf{M}}^\alpha$ is the desired material-aware *boundary–interior transformation matrix*

$$\underset{(2i+2b)\times 2b}{\tilde{\mathbf{M}}^\alpha} = [\ \underset{2b\times 2b}{\mathbf{I}_{2b}}\ ,\ \underset{2i\times 2b}{\mathbf{M}^\alpha}\ ]^T, \tag{29}$$

for a $2b \times 2b$ identity matrix $\mathbf{I}_{2b}$.

3.3. Shape functions in a matrix form

Substituting Eqs. (24) into Eq. (28) further results in

$$\underset{(2i+2b)\times 1}{\mathbf{q}} = \underset{(2i+2b)\times 2b}{\tilde{\mathbf{M}}^\alpha} \; \underset{(2b\times 6r)}{\boldsymbol{\Psi}} \; \underset{(6r\times 1)}{\mathbf{Q}^\alpha}. \tag{30}$$

Further, combining the shape functions $\mathbf{N}^h(\mathbf{x})$ with the local fine mesh $\mathcal{M}^{\alpha,h}$, as defined in Eq. (15), the displacement at any point $\mathbf{x} \in \Omega^\alpha$ is interpolated as

$$\underset{2\times 1}{\mathbf{u}^\alpha(\mathbf{x})} = \underset{2\times(2i+2b)}{\mathbf{N}^h(\mathbf{x})} \; \underset{(2i+2b)\times 1}{\mathbf{q}} = \underset{2\times(2i+2b)}{\mathbf{N}^h(\mathbf{x})} \; \underset{(2i+2b)\times 2b}{\tilde{\mathbf{M}}^\alpha} \; \underset{(2b\times 6r)}{\boldsymbol{\Psi}} \; \underset{(6r\times 1)}{\mathbf{Q}^\alpha}, \quad \mathbf{x} \in \Omega^\alpha. \tag{31}$$

This equation maps the discrete nodal displacement $\mathbf{Q}^\alpha$ to the continuous interpolated displacement $\mathbf{u}^\alpha(\mathbf{x})$. Moreover, it provides the CBN shape functions $\mathbf{N}^\alpha(\mathbf{x})$ in a matrix form,

$$\underset{2\times 6r}{\mathbf{N}^\alpha(\mathbf{x})} = \underset{2\times(2i+2b)}{\mathbf{N}^h(\mathbf{x})} \; \underset{(2i+2b)\times 2b}{\tilde{\mathbf{M}}^\alpha} \; \underset{(2b\times 6r)}{\boldsymbol{\Psi}}, \tag{32}$$

which is determined from the product of the Bézier interpolation matrix $\boldsymbol{\Psi}$ and the boundary–interior transformation matrix $\tilde{\mathbf{M}}^\alpha$.

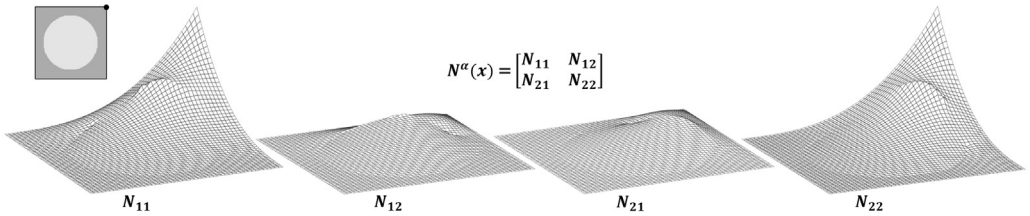

Fig. 6. Surfaces of the four components of the proposed matrix-valued CBN shape function $\mathbf{N}^{\alpha}(\mathbf{x})$ for the corner node in solid; the corner nodes are taken as bridge nodes.

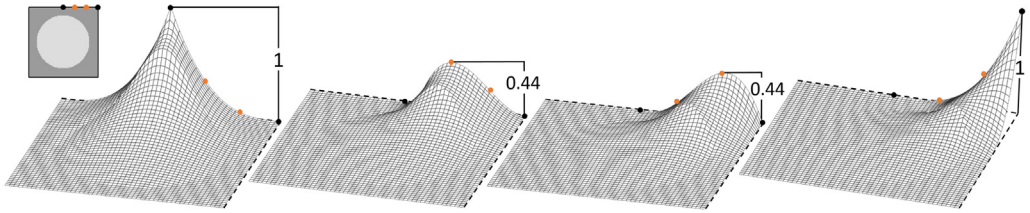

Fig. 7. Shape functions (in their first component) for the four different CBNs; the example has 8 bridge nodes.

The CBN shape functions $\mathbf{N}^{\alpha}(\mathbf{x})$ on the coarse element $\mathcal{M}^{\alpha}$ indicate the assembly of the shape function to each CBN, represented as a 2×2 matrix possibly comprising all non-zero entry values. However, in contrast to the conventional scalar bilinear shape functions where the displacement interpolates each coordinate independently, the matrix-valued shape function tightly couples different dimensions and handles anisotropy naturally; this phenomenon was first observed and studied by [12].

Consider the surface functions in Fig. 6, where the bridge nodes are chosen as the corner nodes. The example has 12 CBNs, and owing to its symmetry, only the shape function to a corner and plot surfaces of its four components are considered. Based on the plots, it is evident that $\mathbf{N}_{11}(\mathbf{x})$ and $\mathbf{N}_{22}(\mathbf{x})$ have much larger height values than those of $\mathbf{N}_{12}(\mathbf{x})$ and $\mathbf{N}_{21}(\mathbf{x})$. This is consistent with the assumption of this study that $\mathbf{N}_{11}(\mathbf{x})$ and $\mathbf{N}_{22}(\mathbf{x})$ play key roles while $\mathbf{N}_{12}(\mathbf{x})$ and $\mathbf{N}_{21}(\mathbf{x})$ regulate the interpolation by coupling different axes. In addition, the complex surfaces in Fig. 7 within a coarse domain differ significantly from the bilinear shape functions and are expected to better expose the heterogeneity of the coarse element.

3.4. Geometric properties of CBN shape functions

The derived CBN shape functions $\mathbf{N}^{\alpha}(\mathbf{x})$ in Eq. (32) also satisfy the basic geometric properties required by FE shape functions to avoid non-physical behavior [12,42,43], including node interpolation, partition of unity (PU), and rotation invariance. This is explained in detail as follows.

Node interpolation. This can be observed as a matrix form of the well-known Lagrange property of the shape functions, or the Kronecker delta function in Eq. (11), which is required for preserving the essential boundary conditions [43]. Specifically, the shape function for node j acquires a value of unity and zero at the other nodes, This property ensures the nodal displacements remain unchanged following the interpolation of the shape functions.

The property can be specified in a matrix form, as follows. Let $\mathbf{Q}_j^{\alpha}$ be the displacement on a coarse node $\mathbf{x}_j$. From the CBN shape function expression in Eq. (32) and the fine nodal displacement expression $\mathbf{q}$ in Eq. (30), the following can be inferred

$$\mathbf{N}^{\alpha}(\mathbf{x}_j)\ \mathbf{Q}^{\alpha} = \mathbf{N}^{h}(\mathbf{x}_j)\ \tilde{\mathbf{M}}^{\alpha}\ \ \boldsymbol{\Psi}\ \mathbf{Q}^{\alpha} = \mathbf{N}^{h}(\mathbf{x}_j)\ \mathbf{q}. \tag{33}$$

Consequently, as the local fine mesh shape functions $\mathbf{N}^{h}(\mathbf{x})$ naturally satisfy the node interpolation property,

$$\mathbf{N}^{h}(\mathbf{x}_j)\ \mathbf{q} = \mathbf{Q}_j^{\alpha}, \tag{34}$$

as does $\mathbf{N}^{\alpha}(\mathbf{x})$, or

$$\mathbf{N}^{\alpha}(\mathbf{x}_j)\ \mathbf{Q}^{\alpha} = \mathbf{Q}_j^{\alpha}, \tag{35}$$

which thus produces a compact matrix form of node interpolation property.

Partition of unity (PU). This property ensures the continuity across the inter-element boundaries [42], enforcing the conformity of the global solution space. Furthermore, PU ensures the property of translation invariance [12], such that the interpolation value at any point maintains relative invariance following the translation.

Here, PU is satisfied for the fine node shape function $\mathbf{N}^h(\mathbf{x})$ and the Bézier interpolation matrix $\boldsymbol{\Psi}$, or

$$\mathbf{N}^h(\mathbf{x})\ \mathbf{I}_{2i+2b,1} = \mathbf{I}_{2,1}, \tag{36}$$

$$\boldsymbol{\Psi}\ \mathbf{I}_{6r,1} = \mathbf{I}_{2b,1}. \tag{37}$$

Substituting $\mathbf{q}_b$ and $\mathbf{q}_i$ with an all-one vector in Eq. (27) gives

$$\mathbf{M}^\alpha\ \mathbf{I}_{2b,1} = \mathbf{I}_{2i,1}, \tag{38}$$

and thus,

$$\tilde{\mathbf{M}}^\alpha\ \mathbf{I}_{2b,1} = [\mathbf{I}_{2b}, \mathbf{M}^\alpha]\ \mathbf{I}_{2b,1} = \mathbf{I}_{2i+2b,1}. \tag{39}$$

Consequently, the PU property for $\mathbf{N}^\alpha(\mathbf{x})$ in a compact matrix form is expressed as

$$\mathbf{N}^\alpha(\mathbf{x})\ \mathbf{I}_{6r,1} = \mathbf{N}^h(\mathbf{x})\ \tilde{\mathbf{M}}^\alpha\ \boldsymbol{\Psi}\ \mathbf{I}_{6r,1} = \mathbf{N}^h(\mathbf{x})\ \tilde{\mathbf{M}}^\alpha\ \mathbf{I}_{2b,1} = \mathbf{N}^h(\mathbf{x})\ \mathbf{I}_{2i+2b,1} = \mathbf{I}_{2,1}. \tag{40}$$

Rotation invariant. This property ensures that the interpolation value at any point maintains relative invariance following geometric rotation. In addition, both PU and rotation invariance improve the robustness of the proposed CBN shape functions.

Specifically, for a constant angular velocity $\hat{\theta}$, the following must hold:

$$\hat{\theta} \times \mathbf{x} = \mathbf{N}^\alpha(\mathbf{x})\ (\hat{\theta} \times \mathbf{x}). \tag{41}$$

The results can be proven similar to the case of the translation invariance by considering that the Bézier curve is rotation invariant and that Eq. (27) is also satisfied under a rotation transformation.

Theorem 1. *The CBN shape functions $\mathbf{N}^\alpha(\mathbf{x})$ in Eq. (32) have the following basic geometric properties:*

$$\mathbf{N}^\alpha(\mathbf{x}_j)\ \mathbf{Q}^\alpha = \mathbf{Q}^\alpha_j,\ \textit{for a coarse node}\ \mathbf{x}_j \in \Omega^\alpha \tag{42}$$

$$\mathbf{N}^\alpha(\mathbf{x})\ \mathbf{I}_{6r,1} = \mathbf{I}_{2,1},\ \ \forall \mathbf{x} \in \Omega^\alpha \tag{43}$$

$$\hat{\theta} \times \mathbf{x} = \mathbf{N}^\alpha(\mathbf{x})\ (\hat{\theta} \times \mathbf{x}),\ \ \forall \hat{\theta},\ \ \mathbf{x} \in \Omega^\alpha, \tag{44}$$

where $\mathbf{Q}^\alpha_j$ is the nodal displacement on CBN nodes and $\hat{\theta}$ is a constant angular velocity.

The properties discussed above are important for producing physically reasonable analysis results using an FE analysis framework. They were imposed as constraints in an optimization problem in a previous study that attempted to construct the material-aware shape functions [12], and are naturally satisfied in the case of the CBN shape functions in this study. The results obtained are summarized as follows.

Theorem 2. *For a coarse element Ω^α, its local fine mesh $\mathcal{M}^{\alpha,h}$, and the fine-mesh shape function $\mathbf{N}^h(\mathbf{x})$ in (15), the CBN shape functions are*

$$\mathbf{N}^\alpha(\mathbf{x}) = \mathbf{N}^h(\mathbf{x})\ \tilde{\mathbf{M}}^\alpha\ \boldsymbol{\Psi}, \tag{45}$$

where the boundary–interior transformation matrix $\tilde{\mathbf{M}}^\alpha$ is defined in Eq. (29) and the Bézier interpolation matrix $\boldsymbol{\Psi}$ is defined in Eq. (25). In addition, the basic geometric properties stated in Theorem 1 are satisfied.

3.5. Numerical aspects

Numerical aspects related to the CBN-based analysis are further discussed in this section, including the computation reduction for CBN shape function construction, and the implementation details on the CBN-based analysis, particularly the numerical computation for the stiffness matrix.

3.5.1. Computation reduction

The main computational costs to derive the shape functions $\mathbf{N}^\alpha(\mathbf{x})$ in Eq. (45) primarily involve the computation of $\mathbf{M}^\alpha$ in Eq. (27), or the product of $\mathbf{k}_i^{-1}$ with $\mathbf{k}_{ib}$. Consequently, it is formulated as a solution to the following linear equation systems:

$$\underset{2i\times 2i}{\mathbf{k}_i}\ \underset{2i\times 2b}{\mathbf{M}^\alpha} = -\underset{2i\times 2b}{\mathbf{k}_{ib}}\,. \tag{46}$$

The column number $2b$ of the right terms can be a very large number, and computing solutions to such excessive equations would be costly, despite the use of a pre-computed LU decomposition. Specifically, it is usually unaffordable as such equation systems have to be computed for all the different coarse elements Ω^α of different stiffness matrices $\mathbf{k}_i$.

The unique introduction of CBNs and the associated Bézier interpolation transformation $\boldsymbol{\Psi}$ in this study provides an alternative that reduces the computational costs. Consequently, multiplying both sides in Eq. (46) by $\boldsymbol{\Psi}$ yields

$$\underset{2i\times 2i}{\mathbf{k}_i}\ \underset{2i\times 2b}{\mathbf{M}^\alpha}\ \underset{2b\times 6r}{\boldsymbol{\Psi}} = -\underset{2i\times 2b}{\mathbf{k}_{ib}}\ \underset{2b\times 6r}{\boldsymbol{\Psi}}\,. \tag{47}$$

Subsequently, instead of computing $\mathbf{M}^\alpha$, the product $\mathbf{M}^\alpha\ \boldsymbol{\Psi}$ is directly computed as the matrix $\boldsymbol{\Phi}$ defined below,

$$\underset{2i\times 2i}{\mathbf{k}_i}\ \underset{2i\times 6r}{\boldsymbol{\Phi}} = \underset{2i\times 2r}{\mathbf{k}_\phi}\,, \quad \text{for} \quad \underset{2i\times 2r}{\mathbf{k}_\phi} = -\underset{2i\times 2b}{\mathbf{k}_{ib}}\ \underset{2b\times 6r}{\boldsymbol{\Psi}}\,. \tag{48}$$

Consequently, the number of linear equation systems to be solved is greatly reduced from $2b$ to a much smaller number of $6r$.

According to Eq. (29), by letting

$$\tilde{\boldsymbol{\Phi}} = [\boldsymbol{\Psi},\ \boldsymbol{\Phi}]^T, \tag{49}$$

the CBN shape function now acquires the following form:

$$\mathbf{N}^\alpha(\mathbf{x}) = \mathbf{N}^h(\mathbf{x})\ \tilde{\boldsymbol{\Phi}}. \tag{50}$$

Corollary 1. *The CBN shape functions $\mathbf{N}^\alpha(\mathbf{x})$ in Theorem 2 can be numerically derived as follows:*

$$\mathbf{N}^\alpha(\mathbf{x}) = \mathbf{N}^h(\mathbf{x})\ \tilde{\boldsymbol{\Phi}}, \tag{51}$$

where $\tilde{\boldsymbol{\Phi}}$ is defined in Eq. (49).

Algorithm 1 Heterogeneous structure analysis using CBN for linear elasticity

Input: a heterogeneous structure Ω, its coarse mesh $\mathcal{M}^H = \{\Omega^\alpha,\ \alpha = 1, 2, \ldots, M\}$, fine mesh $\mathcal{M}^h = \{\omega_e^\alpha,\ e = 1, 2, \ldots, m,\ \alpha = 1, 2, \ldots, M\}$.

Output: the CBN shape functions $\mathbf{N}^\alpha(\mathbf{x})$, and the approximated displacement $\mathbf{Q}$ to Eq. (3)

1: **Prepare** Bézier interpolation matrix $\boldsymbol{\Psi}$ in Eq. (25)
2: **Prepare** boundary–interior transformation matrix $\tilde{\mathbf{M}}^\alpha$ for each coarse element Ω^α in Eq. (29)
3: **Construct** the transformation matrix $\tilde{\boldsymbol{\Phi}}$ in Eq. (48)
4: **Construct** the shape functions $\mathbf{N}^\alpha(\mathbf{x})$ for each Ω^α in Eq. (51)
5: **Compute** the coarse elemental stiffness matrix $\mathbf{K}^\alpha$ based on $\mathbf{K}_e^\alpha$ for each Ω^α in Eq. (56)
6: **Assemble** the global stiffness matrix $\mathbf{K}$
7: **Compute** the displacement solution $\mathbf{Q}$ by Eq. (58)

3.5.2. Heterogeneous structure analysis on CBNs

Upon constructing the CBN shape functions $\mathbf{N}^\alpha(\mathbf{x})$ for each coarse element Ω^α, the displacement to the linear elasticity problem in (3) on a heterogeneous structure Ω can be computed by following a traditional FE analysis framework. The overall algorithm is described in Algorithm 1.

Let $\mathbf{Q}^\alpha$ be the vector of discrete nodal displacements on $\mathcal{M}^H$ to be determined. Then, the continuous displacement $\mathbf{u}^\alpha(\mathbf{x})$ is interpolated using the CBN shape functions $\mathbf{N}^\alpha(\mathbf{x})$,

$$\mathbf{u}^\alpha(\mathbf{x}) = \mathbf{N}^\alpha(\mathbf{x})\ \mathbf{Q}^\alpha. \tag{52}$$

Accordingly, the strain is obtained as

$$\boldsymbol{\varepsilon}^{\alpha}(\mathbf{x}) = \mathbf{B}^{\alpha}(\mathbf{x})\ \mathbf{Q}^{\alpha}, \tag{53}$$

where $\mathbf{B}^{\alpha}(\mathbf{x})$ is the derivative of $\mathbf{N}^{\alpha}(\mathbf{x})$ with respect to $\mathbf{x}$,

$$\mathbf{B}^{\alpha}(\mathbf{x}) = \frac{\partial \mathbf{N}^{\alpha}(\mathbf{x})}{\partial \mathbf{x}} = \frac{\partial \mathbf{N}^{h}(\mathbf{x})}{\partial \mathbf{x}}\ \tilde{\boldsymbol{\Phi}}, \tag{54}$$

according to Eq. (51).

Further, substituting Eq. (53) into the weak formulation Eq. (4), the coarse nodal displacement $\mathbf{Q}$ is computed as

$$\mathbf{K}\ \mathbf{Q} = \mathbf{f}, \quad \text{for} \quad \mathbf{K} = \sum_{\alpha=1}^{M} \mathbf{K}^{\alpha}, \tag{55}$$

where

$$\begin{aligned}
\mathbf{K}^{\alpha} &= \int_{\Omega^{\alpha}} (\mathbf{B}^{\alpha}(\mathbf{x}))^{T}\ \mathbf{D}(\mathbf{x})\ \mathbf{B}^{\alpha}(\mathbf{x})\ \mathrm{d}\Omega^{\alpha} \\
&= \sum_{e=1}^{m} \int_{\omega_e} (\mathbf{B}^{\alpha}(\mathbf{x}))^{T}\ \mathbf{D}_e(\mathbf{x})\ \mathbf{B}^{\alpha}(\mathbf{x})\ \mathrm{d}\omega_e \\
&= \sum_{e=1}^{m} \tilde{\boldsymbol{\Phi}}^{T} \Big(\int_{\omega_e} \big(\frac{\partial \mathbf{N}^{h}(\mathbf{x})}{\partial \mathbf{x}}\big)^{T}\ \mathbf{D}_e(\mathbf{x})\ \frac{\partial \mathbf{N}^{h}(\mathbf{x})}{\partial \mathbf{x}}\ \mathrm{d}\omega_e \Big)\ \tilde{\boldsymbol{\Phi}} \\
&= \sum_{e=1}^{m} \mathbf{K}_e^{\alpha},
\end{aligned} \tag{56}$$

for

$$\mathbf{K}_e^{\alpha} = \tilde{\boldsymbol{\Phi}}^{T} \Big(\int_{\omega_e} \big(\frac{\partial \mathbf{N}^{h}(\mathbf{x})}{\partial \mathbf{x}}\big)^{T}\ \mathbf{D}_e(\mathbf{x})\ \frac{\partial \mathbf{N}^{h}(\mathbf{x})}{\partial \mathbf{x}}\ \mathrm{d}\omega_e \Big)\ \tilde{\boldsymbol{\Phi}}, \tag{57}$$

by noticing Eq. (54).

Numerical computation for $\mathbf{K}^{\alpha}$. The computation of $\mathbf{K}^{\alpha}$ involves an integration computation on a coarse element Ω^{α}. In the case of a homogeneous Ω^{α}, it is computed using Gauss integration at 2^d Gauss points, $d = 2, 3$. However, the integration works on a heterogeneous coarse element Ω^{α} and a piecewise shape function $\mathbf{N}^{\alpha}(\mathbf{x})$. Thus, to achieve computation accuracy, the integration must be conducted on each fine element ω_e and assembled together following Eq. (56). Further, additional 2^d Gauss points, $d = 2, 3$, are considered for each fine element. Moreover, $\mathbf{N}^{h}(\mathbf{x})$ is locally supported, and the numerical integration in Eq. (57) only involves $\mathbf{N}_e(\mathbf{x})$ instead of $\mathbf{N}^{h}(\mathbf{x})$ for a specific fine element ω_e.

Corollary 2. *Let Ω be a heterogeneous solid structure and $\mathcal{M}^{H}, \mathcal{M}^{\alpha,h}$ be its coarse and fine meshes, respectively. Then, the solution $\mathbf{Q}$ to the linear elasticity analysis problem in Eq. (3) can be computed as*

$$\mathbf{K}\ \mathbf{Q} = \mathbf{f}, \tag{58}$$

for

$$\mathbf{K} = \sum_{\alpha=1}^{M} \mathbf{K}^{\alpha} = \sum_{\alpha=1}^{M} \sum_{e=1}^{m} \mathbf{K}_e^{\alpha}, \tag{59}$$

and $\mathbf{K}_e^{\alpha}$ given in (57).

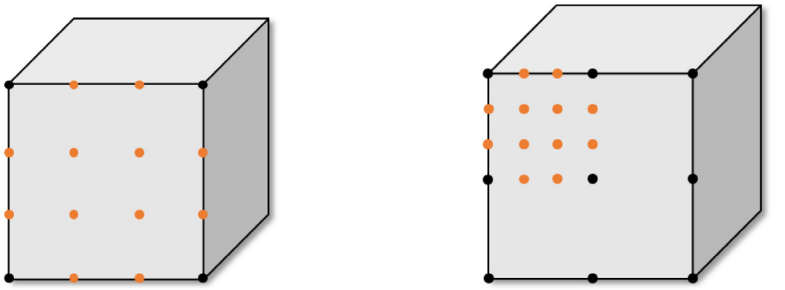

(a) Corner nodes as bridge nodes, $\mathcal{X}_c = \mathcal{X}_r$ (b) 3×3 bridge nodes, $\mathcal{X}_c \subset \mathcal{X}_r$

Fig. 8. Strategies to set CBN in 3D cases for shape function construction.

4. Extension to 3D cases and nonlinear analysis

4.1. Extension to 3D cases

In this section, the CBN shape functions are extended to 3D cases, primarily on the construction of the Bézier interpolation matrix $\boldsymbol{\Psi}$ and boundary–interior transformation matrix $\tilde{\mathbf{M}}^{\alpha}$. Specifically, $\boldsymbol{\Psi}$ is extended from cubic Bézier curves to bicubic Bézier surfaces, whereas $\tilde{\mathbf{M}}^{\alpha}$ is extended from 2D FE analysis to 3D FE analysis.

4.1.1. 3D Bézier interpolation matrix $\boldsymbol{\Psi}$

In 3D case, the bicubic Bézier surface is formed as

$$\mathbf{P}(\mathbf{t}) = \sum_{i=0}^{3}\sum_{j=0}^{3} \psi_i(t_u)\ \psi_j(t_v)\ \mathbf{P}_{ij} = \sum_{i=0}^{3}\sum_{j=0}^{3} C_3^i t_u^i (1-t_u)^{3-i}\ C_3^j t_v^j (1-t_v)^{3-j}\ \mathbf{P}_{ij}, \tag{60}$$

where $\mathbf{t} = (t_u, t_v)$, $\mathbf{P}_{ij} \in \mathbb{R}^3$ is the control point, $\psi_i(t_u)$ or $\psi_j(t_v)$ is a cubic Bernstein basis, and C_3^i is the binomial coefficient.

In a similar manner, $\mathbf{P}(\mathbf{t})$ can be written in a matrix form as

$$\underset{(3\times 1)}{\mathbf{P}(\mathbf{t})} = \underset{(3\times 48)}{\boldsymbol{\psi}_F(t_u, t_v)} \quad \underset{(48\times 1)}{\mathbf{P}} \tag{61}$$

for

$$\mathbf{P} = [\mathbf{P}_0, \mathbf{P}_1, \ldots, \mathbf{P}_{15}]^T, \quad \boldsymbol{\psi}_F = \boldsymbol{\psi}_1(t_u)\ \boldsymbol{\psi}_2(t_v), \tag{62}$$

and

$$\underset{(3\times 12)}{\boldsymbol{\psi}_1(t_u)} = \underset{(1\times 4)}{\boldsymbol{\psi}_0(t_u)} \otimes \underset{(3\times 3)}{\mathbf{I}_3}\ , \quad \underset{(12\times 48)}{\boldsymbol{\psi}_2(t_v)} = \underset{(1\times 4)}{\boldsymbol{\psi}_0(t_v)} \otimes \underset{(12\times 12)}{\mathbf{I}_{12}}\ , \tag{63}$$

where $\boldsymbol{\psi}_0(t)$ is referred to in Eq. (21)

For a particular face F determined by a set of bridge nodes, similar to the 2D case, the displacement on any point $\mathbf{x}$ on face F is obtained as

$$\mathbf{u}_F(\mathbf{x}) = \mathbf{u}(t_u(\mathbf{x}), t_v(\mathbf{x})) = \boldsymbol{\psi}_F(t_u(\mathbf{x}), t_v(\mathbf{x}))\ \mathbf{Q}_F, \tag{64}$$

where $\mathbf{Q}_F$ is the vector of the displacements on the associated CBNs, as indicated in Fig. 8.

Subsequently, assembling $\mathbf{u}_F(\mathbf{x})$ over all faces F and evaluating it on all the boundary nodes in $\mathcal{X}_b$, the 3D Bézier interpolation matrix is expressed as

$$\underset{(3b\times q)}{\boldsymbol{\Psi}} = \left[\sum_F \boldsymbol{\psi}_F(\mathbf{t}(\mathbf{x}_0)),\ \ \mathbf{x}_0 \in \mathcal{X}_b\right], \tag{65}$$

where q is the number of DOFs on CBNs, given as

$$q = 3\ (54x^2 - 108x + 56) \quad \text{for} \quad x = 1 + \frac{1}{6}\sqrt{6r - 12}. \tag{66}$$

4.1.2. Boundary–interior transformation matrix $\tilde{\mathbf{M}}^{\alpha}$

In the 3D case, the shape function matrix $\mathbf{N}_e(\mathbf{x})$ has a dimension of 3×24 in the following form:

$$\mathbf{N}_e(\mathbf{x}) = \left[\begin{array}{cccccccc} \mathbf{N}_1(\mathbf{x}) & \mathbf{N}_2(\mathbf{x}) & \mathbf{N}_3(\mathbf{x}) & \mathbf{N}_4(\mathbf{x}) & \mathbf{N}_5(\mathbf{x}) & \mathbf{N}_6(\mathbf{x}) & \mathbf{N}_6(\mathbf{x}) & \mathbf{N}_8(\mathbf{x}) \end{array} \right], \tag{67}$$

where each submatrix $\mathbf{N}_i(\mathbf{x})$ is

$$\mathbf{N}_i(\mathbf{x}) = \left[\begin{array}{ccc} N_i(x) & 0 & 0 \\ 0 & N_i(y) & 0 \\ 0 & 0 & N_i(z) \end{array} \right], \tag{68}$$

and $N_i(\mathbf{x})$ is the *trilinear shape function* defined on each of the eight corner nodes,

$$N_i(\mathbf{x}) = \frac{1}{8}(1 + x_i x)(1 + y_i y)(1 + z_i z) \quad , 1 \le i \le 8, \quad (x, y, z) \in [-1, 1] \times [-1, 1] \times [-1, 1]. \tag{69}$$

Consequently, following the approach similar to the 2D case, the boundary–interior transformation matrix $\tilde{\mathbf{M}}^{\alpha}$ can be derived.

4.2. Extension to nonlinear analysis

The extension of the proposed approach to nonlinear analysis is discussed herein, specifically focusing on neo-Hookean elasticity. For this study, only the bilinear or trilinear shape functions for each coarse element Ω^{α} need to be replaced with the proposed CBN shape functions $\mathbf{N}^{\alpha}(\mathbf{x})$ in the deformation gradient $\mathbf{F}(\mathbf{x})$, as follows

$$\mathbf{F}(\mathbf{x}) = \frac{\partial \mathbf{u}(\mathbf{x})}{\partial \mathbf{X}} + \mathbf{I}_d = \frac{\partial \mathbf{N}^{\alpha}(\mathbf{x})}{\partial \mathbf{X}} \mathbf{Q}^{\alpha} + \mathbf{I}_d, \tag{70}$$

where $\mathbf{x}$ is in the deformed shape, $\mathbf{X}$ is in the reference shape, and $\mathbf{I}_d$ is a $d \times d$ identity matrix for $d = 2, 3$.

Subsequently, a nonlinear elasticity analysis can be conducted using the deformation gradients $\mathbf{F}(\mathbf{x})$, following a classical nonlinear FE analysis process [44]. The overall algorithm is described in Algorithm 2. The iterations in the coarse mesh analysis all work on an undeformed regular mesh, and thus, the CBN-shape functions are only generated once at the beginning (in Step 2). In addition, the fine mesh field solution needs to be reconstructed during the iteration (in Step 6) from the coarse mesh solution, because the material property on each fine mesh $\mathbf{D}_e(\mathbf{x})$ in Eq. (56) is dependent on the solution $\mathbf{u}$, or $\mathbf{D}_e(\mathbf{u}, \mathbf{x})$, and must therefore be updated during the iterations.

Comment. Depending on the different nonlinear analysis approaches, the CBN-based shape functions may be reconstructed during the iteration for improved analysis accuracy, although at the cost of considerable computational efficiency loss. In addition, constructing the CBN shape functions via linear analysis, as in this study, cannot fully describe the nonlinear behavior of a coarse element, and in general, results in the loss of certain analysis accuracy. Thus, devising a more advanced CBN shape function from nonlinear elasticity analysis is expected to overcome the challenge, and is under the purview of this study. The performance of the CBN-based shape functions for nonlinear analysis is further demonstrated in Section 6.7.

Accuracy improvement in nonlinear cases. To improve the elastic behaviors of the nonlinear model, the following corotational formulation [12] of the displacement was considered

$$\mathbf{u}(\mathbf{x}) = \mathbf{R}^{\alpha}(\mathbf{X} + \mathbf{N}^{\alpha}(\mathbf{x})(\mathbf{R}^{\alpha}\mathbf{x} - \mathbf{X})) - \mathbf{X}, \tag{71}$$

where $\mathbf{R}^{\alpha}$ is the local frame to each shape function [12].

5. Discussions

This section presents an extended discussion of the relation and difference between the proposed CBN analysis approach (denoted CBN) and certain previous classical approaches for heterogeneous structure analysis: Homogenization [25,26], FE^2 using Voigt–Taylor model [34], the second-order CMCM [21] (CMCM for short), and Substructuring [36].

Algorithm 2 Heterogeneous structure analysis using CBN for nonlinear elasticity

Input: a heterogeneous structure Ω, its coarse mesh $\mathcal{M}^H = \{\Omega^\alpha,\ \alpha = 1, 2, \ldots, M\}$, fine mesh $\mathcal{M}^h = \{\omega_e^\alpha,\ e = 1, 2, \ldots, m,\ \alpha = 1, 2, \ldots, M\}$.

Output: the CBN shape functions $\mathbf{N}^\alpha(\mathbf{x})$, and the approximated displacement $\mathbf{Q}$ to Eq. (3)

Initialize the displacement $\mathbf{Q} = 0$
Construct the shape functions $\mathbf{N}^\alpha(\mathbf{x})$ following steps 1–4 in Algorithm 1
while unconverged **do**
    Compute the corotational matrix $\mathbf{R}^\alpha$ for each Ω^α
    Compute the deformation gradient $\mathbf{F}(\mathbf{x})$ for each Ω^α in Eq. (70)
    Compute the displacements $\mathbf{q}$ on the fine field based on the current $\mathbf{Q}$ and $\mathbf{N}^\alpha(\mathbf{x})$
    Compute the coarse elemental stiffness matrix $\mathbf{K}^\alpha$ based on $\mathbf{K}_e^\alpha$ for each Ω^α in Eq. (56)
    Assemble the global stiffness matrix $\mathbf{K}$
    Compute the elastic forces $\mathbf{f}_{int}$
    Compute the residual forces $\Delta\mathbf{f} = \mathbf{f}_{ext} - \mathbf{f}_{int}$
    Compute the increment of displacement $\Delta\mathbf{Q} = \mathbf{K}^{-1}\Delta\mathbf{f}$
    Compute the step size t using line-search
    Update the displacement $\mathbf{Q} += t\,\Delta\mathbf{Q}$

5.1. Technical differences

In general, most approaches, including Homogenization, CMCM, Substructuring, and the proposed CBN, conduct the analysis following two main procedures: an offline process to compute local fine mesh displacement for each coarse element, and an online process to conduct the global analysis on the coarse mesh. In contrast, FE^2 follows a different process, where both local and global analyses are iteratively conducted online. Here, the *offline* is termed in the sense that the CBN shape functions can be derived in parallel through offline calculations, following previous naming [21]. In addition, the offline calculation is dependent on a specific heterogeneous structure, irrespective of varied loading conditions. Fig. 9 shows an illustration of the flowcharts of these approaches, with their differences explained below.

Scale separation assumption. Homogenization assumes scale separation as a precondition, and thus, results in a loss of much of its analysis accuracy if the assumption is broken. In contrast, other approaches, including the FE^2 of Voigt–Taylor model, Substructuring, CMCM and CBN, are not based on this assumption.

Local computations. All the local computations involve solution computations to linear equation systems of the same left-hand stiffness matrix. However, the right hand is different in two aspects: the number of columns and the entry values. The column number is determined by the involved coarse analysis DOFs. Further, the entry values are calculated from the imposed boundary conditions: testing BCs in Homogenization and CMCM, linear interpolation of coarse corner displacements in FE^2, or a submatrix of the local fine-mesh stiffness matrix in Substructuring and CBN.

Fine–coarse transmission. Homogenization or FE^2 transmit specific physical quantities for global coarse-mesh analysis, such as an effective material elasticity tensor and internal force vector. In addition, FE^2 attempts to further improve the analysis accuracy via iterative computations between the local fine and coarse meshes, and may consequently encounter a convergence issue. In contrast, Substructuring, CMCM or CBN constructs an explicit physical field, specifically strain fields or the derivatives of the shape functions, local stiffness matrix of the super-elements, and CBN shape functions. Subsequently, they are used to generate the local stiffness matrix to the coarse element.

Global solution reconstruction. For a particular coarse mesh solution, reconstructing the local response in the local fine mesh is important for various industrial applications. However, Homogenization only computes the coarse displacement and is not directly applicable to recover the fine-mesh displacement. In contrast, the other approaches studied here can reconstruct the fine-mesh strain or stress field directly. Regarding global displacement smoothness,

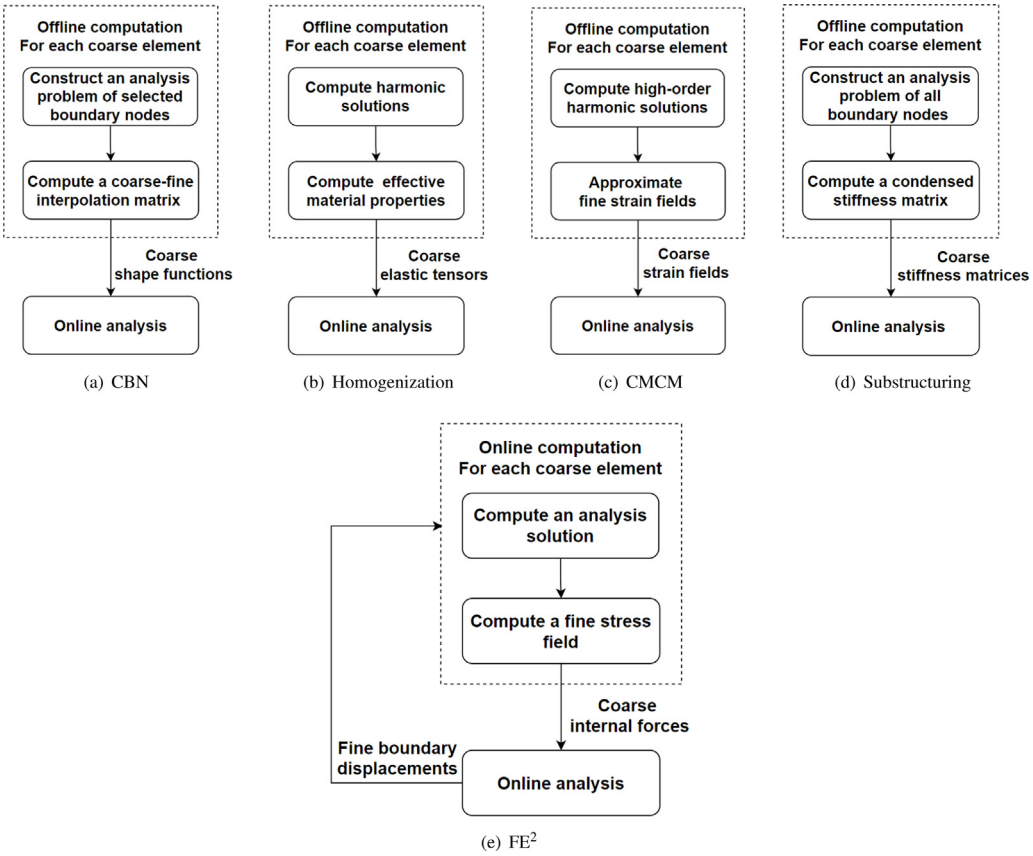

Fig. 9. Flowcharts of different approaches for heterogeneous structure analysis, including CBN, Homogenization, CMCM, Substructuring and FE^2.

CMCM is not continuous along the coarse boundary as its coarse strain fields are constructed locally without adjacency consideration; in contrast, the other three approaches, Substructuring, FE^2, and CBN, can generate a globally smooth displacement, although they each have significantly different computational costs, as discussed later in this paper.

5.2. Complexity analysis

The complexity primarily depends on two aspects: local displacement computation to each coarse element and the global displacement computation on the coarse mesh, which has been further analyzed below.

5.2.1. Complexity analysis of local displacement computations

For all the approaches mentioned above, the local analysis problem involves all the efforts to compute displacements $\bar{\mathbf{q}}$ to a set of linear equation systems as

$$\mathbf{k}_i \ \bar{\mathbf{q}} = \bar{\mathbf{f}}, \tag{72}$$

where $\mathbf{k}_i$ is the submatrix defined in Eq. (26), and $\bar{\mathbf{f}}$ represents a set of column vectors.

Let κ be the number of vectors, which determines the number of equation systems to be computed, and consequently, the computational complexity (Table 2). In the case of Homogenization and CMCM, κ is dependent on the number of testing boundaries: 3 in 2D or 6 in 3D in Homogenization, and 5 in 2D and 15 in 3D in CMCM (as CMCM imposes high-order boundary conditions). Regarding Substructuring, it is $\kappa = 2b$ in 2D or $3b$ in 3D, which typically can be as high as tens of thousands. Further, in the case of the proposed CBN, $\kappa = 6r$ in 2D or q

Table 2
Computational complexity comparisons of different heterogeneous structure analysis approaches: Homogenization, FE^2, CMCM, Substructuring, and CBN.

Methods	Number of linear equation systems for each coarse element (2D or 3D)	DOFs of each coarse element in online analysis (2D or 3D)
Homogenization	3 or 6	8 or 24
FE^2	1 for one iteration	8 or 24
CMCM	5 or 15	8 or 24
Substructuring	$2b$ or $3b$	$2b$ or $3b$
CBN	$6r$ or q	6r or q

b is the number of boundary nodes in $\mathcal{X}_b$, r is the number of coarse bridge nodes in $\mathcal{X}_r$, and q is expressed in Eq. (66).

Table 3
Parameter setting of all the numerical examples in the study.

Model	Young's modulus		Coarse mesh	Local fine mesh	Bridge nodes per edge/face
	Matrices	Inclusions			
Half MBB of Fig. 12	$1e^3$	1	2×4	10×10	2
Half MBB of Fig. 13(a)	$1e^3$	1	2×4	64×64	–
Half MBB of Fig. 13(b)	$1e^3$	1	–	–	2
Half MBB of Fig. 13(c)	–	–	2×4	64×64	2
Half MBB of Fig. 16	–	–	2×2	50×50	2
Half MBB of Fig. 17	1	$1e^3$	2×2	50×50	2
Bending beam of Fig. 18	$1e^3$	1	–	–	2
3D example of Fig. 21	$1e^4$	$1e^3$	$2 \times 2 \times 8$	$10 \times 10 \times 10$	3×3
Geologic model of Fig. 23	–	–	$20 \times 30 \times 42$	$30 \times 30 \times 30$	2×2

– denotes the parameter with different values could be referred in the corresponding section.

(in Eq. (66)) in 3D, which is typically in the hundreds. Finally, for FE^2, κ is equal to the number of iterations; it only has a single column vector in each iteration.

Moreover, these different linear equation systems all possess the same left-hand matrix, and thus, the displacements to different right-hand column vectors can be efficiently computed by performing KL-decomposition in advance. However, this strategy is not directly applicable in the case of FE^2.

5.2.2. Complexity analysis of global displacement computation

The complexity is determined by the DOFs in each coarse element. Homogenization, CMCM or FE^2 analysis only involves the corner nodes and has node numbers of 8 in 2D or 24 in 3D; Substructuring has DOFs of $2b$ in 2D or $3b$ in 3D. Moreover, CBN has the number of $6r$ in 2D or q in 3D. The complexity analysis results are summarized in Table 2.

For a more intuitive perspective, Fig. 10 shows the plots of the sparsity of the global stiffness matrix of each method. Here, the coarse mesh exhibits a dimension of 2×4, whereas the local fine mesh exhibits a dimension of 10×10, and the analysis results on the global fine mesh are considered the benchmark. Moreover, even in the case of this simple example, Substructuring has a dense stiffness matrix, and its number of nonzero elements is approximately 1.5 times that of the benchmark. Thus, its direct use on large-scale industrial application problems may be impractical. In contrast, the proposed CBN approach significantly reduces the number by introducing a Bézier interpolation matrix.

6. Experiments

The proposed approach of CBN heterogeneous structure analysis was implemented in MATLAB on an Intel Core i7, 3.7 GHz CPU and 64 GB RAM PC. The performance was tested on various 2D and 3D examples. The parameter settings of all these examples are summarized in Table 3 for clarity. Further, for illustration purposes, the geometry, material, and load data were chosen to be dimensionless. In addition, in all the examples, if not specifically stated, the matrices were assumed with Young's modulus $E = 1e^3$ and the inclusions of $E = 1$; both

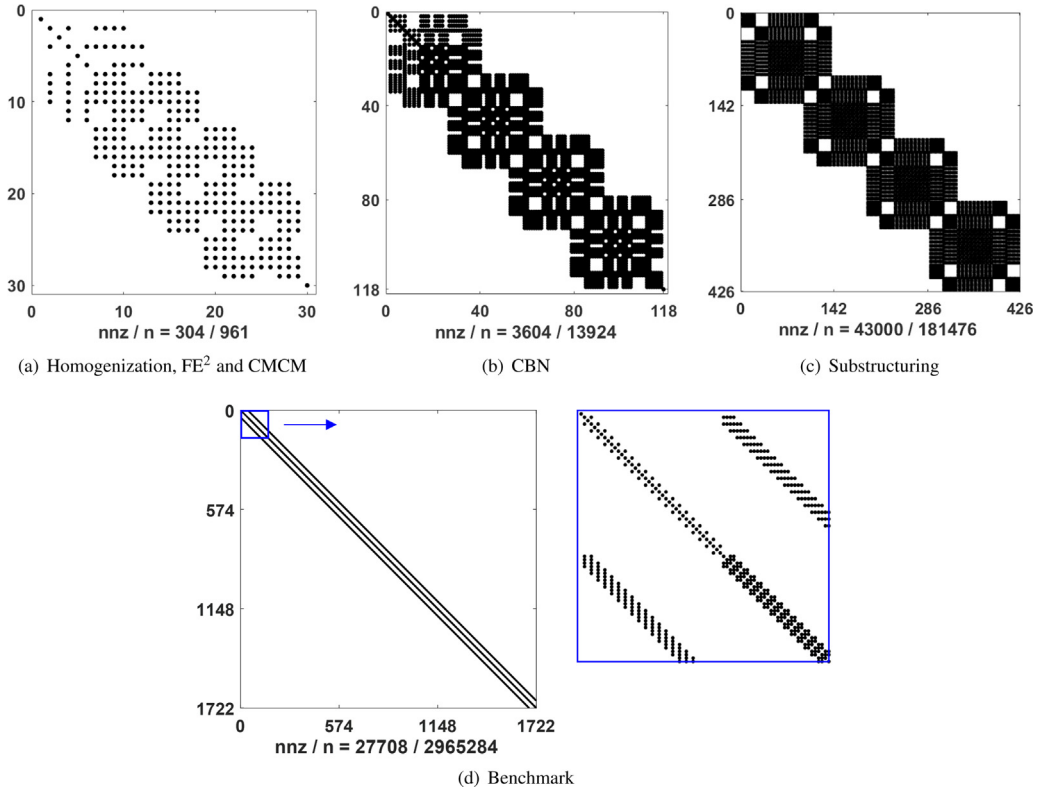

(a) Homogenization, FE^2 and CMCM (b) CBN (c) Substructuring

(d) Benchmark

Fig. 10. Plots of the sparsities of the global stiffness matrices for different heterogeneous structure analysis approaches: Homogenization, CMCM, FE^2, Substructuring and CBN. Here, nnz denotes the number of non-zero values, and n is the size of the matrix. Note that nnz of Substructuring is approximately 1.5 times that of the benchmark.

had a Poisson's ratio of $\mu = 0.3$. However, under these settings, the heterogeneous structures tended to present a large deformation, of which analyzing with a high level of accuracy was challenging. Furthermore, the bridge nodes were all set as the corner nodes by default.

The Substructuring approach is not discussed as it constantly produced solutions of high accuracy with significantly high computational costs for large-size problems (complexity analysis in Section 5.2). Here, *LBN* and *CBN* were used to denote the approaches proposed in this study using linear interpolation or cubic Bézier interpolation, respectively; both have the same number of analysis DOFs to facilitate a fair comparison.

The analysis result on the global fine mesh $\mathcal{M}^h$ was considered the benchmark, where the fine mesh conformed to the heterogeneities in all the examples, that is, each fine element was only filled with a single type of material. Further the boundary conditions and the loading forces of all the benchmarks were consistent with the corresponding coarse meshes. Regarding the global energy or displacement, the analysis fidelity was measured via *effectivity index* as the relative variation in the computed result with respect to the benchmark.

$$r_e = \frac{(e_1 - e_0)^2}{e_0^2}, \quad r_u = \frac{\int_\Omega (\mathbf{u}_1 - \mathbf{u}_0)^2 \, d\Omega}{\int_\Omega \mathbf{u}_0^2 \, d\Omega}, \tag{73}$$

where e_1, e_0 are the computed and the benchmark energies, respectively, and $\mathbf{u}_1, \mathbf{u}_0$ are the computed and the benchmark displacements, respectively.

6.1. Overall performance and comparisons with related approaches

The overall performance and its comparison with related approaches including, Homogenization [25,26], FE^2 using Voigt–Taylor model [34], the second-order CMCM [21], and LBN using direct interpolation, is presented in

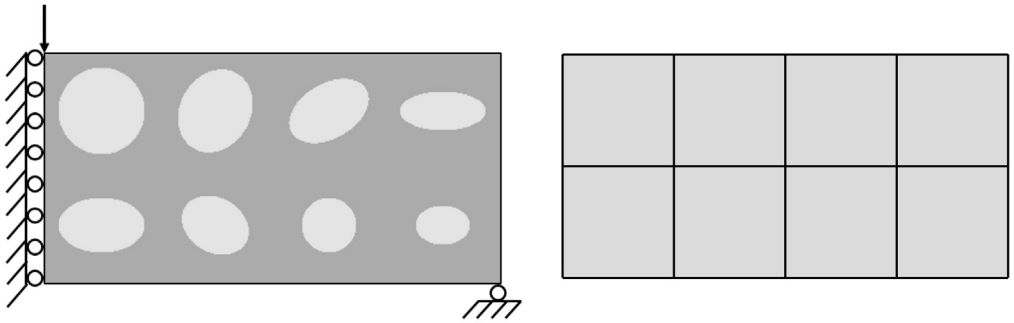

(a) Half MBB (b) Coarse mesh $\mathcal{M}^H$ of 2×4

Fig. 11. Half MBB example has 2×4 coarse elements, each containing an elliptic inclusion.

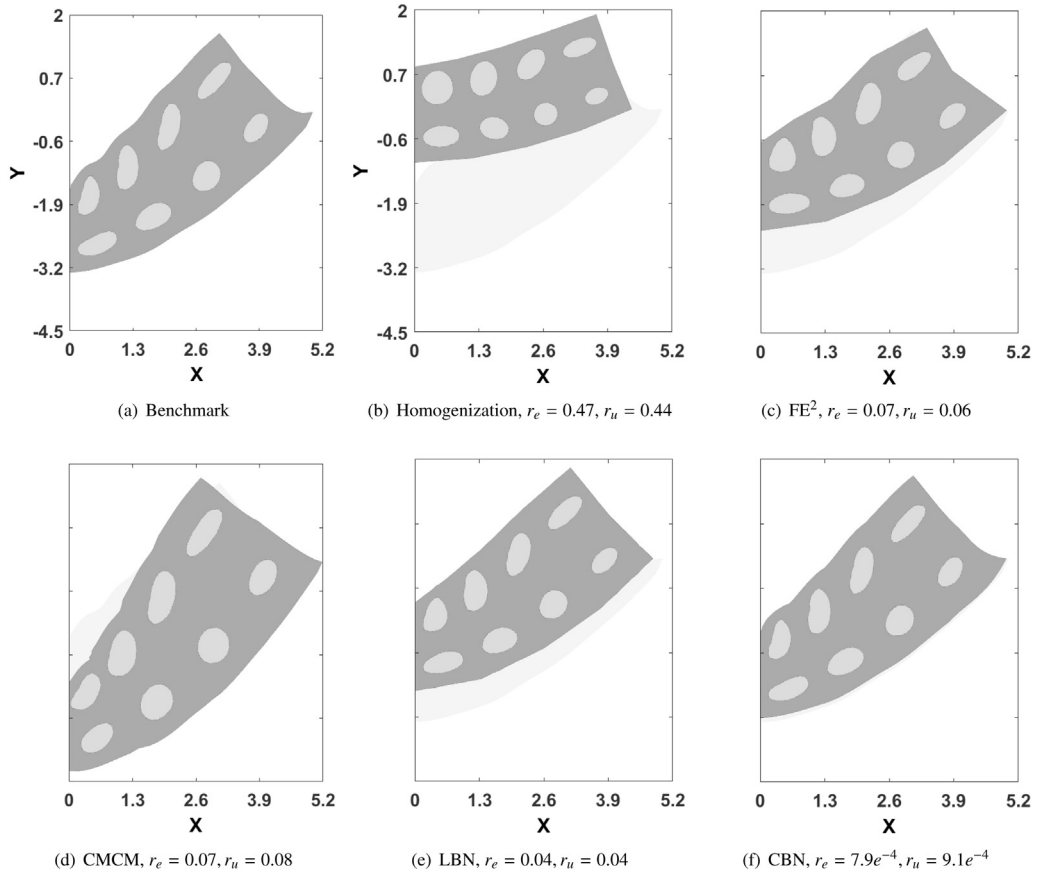

(a) Benchmark (b) Homogenization, $r_e = 0.47, r_u = 0.44$ (c) FE^2, $r_e = 0.07, r_u = 0.06$

(d) CMCM, $r_e = 0.07, r_u = 0.08$ (e) LBN, $r_e = 0.04, r_u = 0.04$ (f) CBN, $r_e = 7.9e^{-4}, r_u = 9.1e^{-4}$

Fig. 12. Numerical results of the heterogeneous half MBB example in Fig. 11 compared with benchmark and other related approaches: Homogenization, FE^2, CMCM, and LBN, where the shadow areas denote the benchmark deformations.

this section. The test was conducted on the half heterogeneous MBB example in Fig. 11. The coarse mesh size was 2×4, and that of the local fine mesh was 10×10. The results are summarized in Fig. 12 and Table 4.

The reconstructed deformation for each approach is shown in Fig. 12 with the effective indices r_e and r_u. Large deformation differences were clearly observed between results of the benchmark and Homogenization, FE^2, CMCM, and LBN. In contrast, CBN exhibited a deformation almost identical to that of the benchmark, even at the local regions of large deformation. Further, their effectivity indices indicated similar phenomena: Homogenization yielded

Table 4
Approach timings (in s): Homogenization, FE^2, CMCM, LBN, and CBN for the half MBB example in Fig. 11.

Approaches	Solving linear equations systems for each coarse element	Solving $\mathbf{KU} = \mathbf{F}$ in online analysis
Benchmark	–	0.21
Homogenization	$3.2e^{-4}$	$4e^{-3}$
FE^2	$3.2e^{-4}$	$4e^{-3}\times$ 13[a]
CMCM	$3.3e^{-4}$	$4e^{-3}$
LBN	$4.3e^{-4}$	$5e^{-3}$
CBN	$4.3e^{-4}$	$5e^{-3}$

[a]FE^2 has 13 iterations in this example.

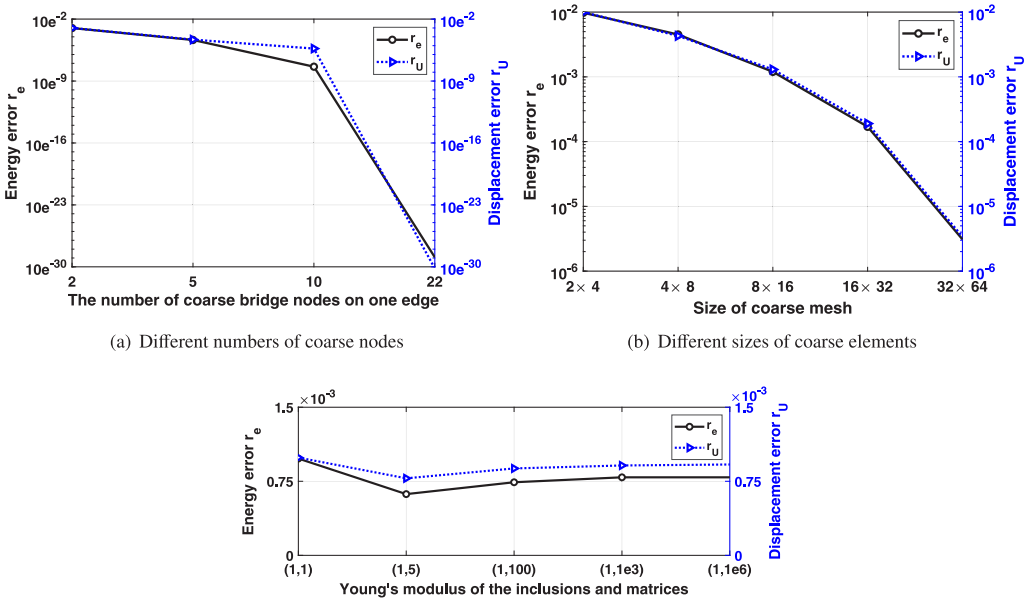

(a) Different numbers of coarse nodes

(b) Different sizes of coarse elements

(c) Different material contrasts

Fig. 13. Variations in effectivity indices r_e, r_u under different mesh settings.

the largest index of 0.47, CBN the smallest of $7.9e^{-4}$, and FE^2, CMCM, and LBN have an index of approximately 0.07. Thus, a two-order improvement was observed using CBN. Moreover, Homogenization, FE^2, and LBN tended to over-stiffen the deformation, whereas CMCM tended to soften it in this example.

The time costs are summarized in Table 4. As indicated, the benchmark required the longest time, whereas the other approaches reduced it dramatically. In the local analysis for a coarse element, different approaches exhibited similar timings, although CBN and LBN required slightly more time; the local computations could be conducted in parallel online except for FE^2. In online computation of the global coarse displacement, FE^2 required more time than the other approaches as it required 13 iterations. LBN and CBN required more time than Homogenization and CMCM, and this difference may further increase in case of super large-sized analysis problems. Thus, the numerical results are consistent with the algorithmic complexity analysis in Section 5.2.

6.2. Performance at different mesh settings

The performance of CBN was further tested at different analysis parameters: size of coarse mesh and number of bridge nodes or contrast of material stiffnesses. The half MBB in Fig. 11 was used here, where the coarse mesh size was 2 × 4, and the local fine mesh size was 64 × 64. The results are presented in Fig. 13.

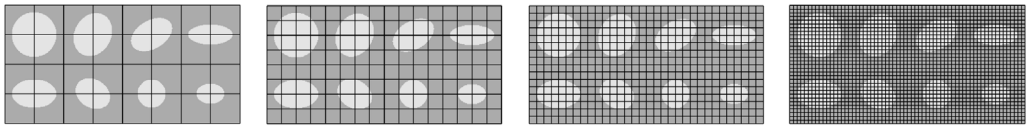

(a) $\mathcal{M}^H$ of 4×8 (b) $\mathcal{M}^H$ of 8×16 (c) $\mathcal{M}^H$ of 16×32 (d) $\mathcal{M}^H$ of 32×64

Fig. 14. Different coarse mesh sizes are set for the half MBB in Fig. 11.

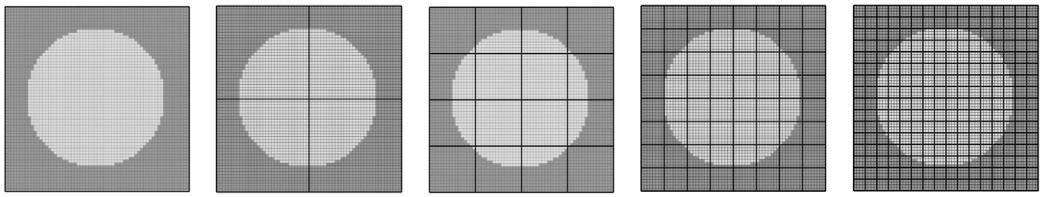

(a) On $\mathcal{M}^H$ of 2×4 (b) On $\mathcal{M}^H$ of 4×8 (c) On $\mathcal{M}^H$ of 8×16 (d) On $\mathcal{M}^H$ of 16×32 (e) On $\mathcal{M}^H$ of 32×64

Fig. 15. Part of the used fine meshes for the MBB example in Fig. 11 at different coarse mesh size.

Different numbers of bridge nodes $\mathcal{X}_r$. CBN offers the unique ability of choosing different numbers of bridge nodes. Its performance was tested at bridge node numbers of $2, 5, 10, 22$ along a boundary, and Fig. 13(a) shows their effectivity indices r_e and r_u. The indices were observed to decrease rapidly with an increase in the bridge node number, and particularly exhibited a very high accuracy of $r_e = 1.2e^{-28}$ and $r_u = 6.7e^{-30}$ in the case of 22 bridge nodes. In this case, the CBN number is equal to the number of all boundary nodes, and CBN essentially conducts an identical analysis to the benchmark on the global fine mesh.

Different sizes of coarse meshes $\mathcal{M}^H$. As indicated in Fig. 14, five different sizes of coarse mesh $\mathcal{M}^H$ 2×4, 4×8, 8×16, 16×32, and 32×64 were set, while the global fine mesh size was unchanged as 128×256. In addition, Fig. 15 shows the plots of part of the fine meshes of the five differently sized coarse meshes for illustration. The fine mesh conformed to the inclusion heterogeneities such that each fine element was only filled with a single type of material. Here, excluding the case of 2×4, the coarse mesh boundaries crossed the different interface materials. Further, the dramatic material variations along the boundaries posed a significant challenge in terms of maintaining analysis accuracy. However, the proposed approach still demonstrates its high performance, as indicated by the effectivity indices in Fig. 13(b).

Different contrasts of material stiffness. Different contrasts of Young's modulus were respectively set for the inclusions and matrices: $(1, 1)$, $(1, 5)$, $(1, 100)$, $(1, 1e^3)$, $(1, 1e^6)$. The derived effectivity indices are plotted in Fig. 13(c). In general, the larger the ratios, the more difficult it was to achieve a reasonable result, considering the fact that the relatively softer inclusion tensors tended to exhibit a large local deformation. Yet, CBN can maintain a high analysis accuracy of all effectivity indices below $1e^{-3}$, even for the extreme ratio of $(1, 1e^6)$.

Moreover, the index at $(1, 1)$ was slightly larger than the other indices, which appears to be different from that expected intuitively. In fact, the accuracy of the CBN shape functions is determined by its ability to approximate the heterogeneous model deformations. The ability, on the one hand, is influenced by the structural heterogeneity; on the other hand, it is influenced by the local deformation behaviors. However, the case of $(1, 1)$, despite homogeneous material distribution, has a much smaller Young's modulus overall, and thus, the model may still tend to produce a larger deformation, possibly inducing additional errors.

6.3. Shape functions in terms of material distributions

The constructed CBN shape functions are expected to closely reflect the interior material distributions for high accuracy analysis, irrespective of the imposed boundary conditions. This was tested by plotting in Fig. 16 the surfaces of the CBN shape functions for the cases of different material distributions. The local fine mesh size was 50×50, and the corner nodes were regarded as bridge nodes. Further, their associated effectivity indices on a 2×2 coarse mesh are shown below each shape function.

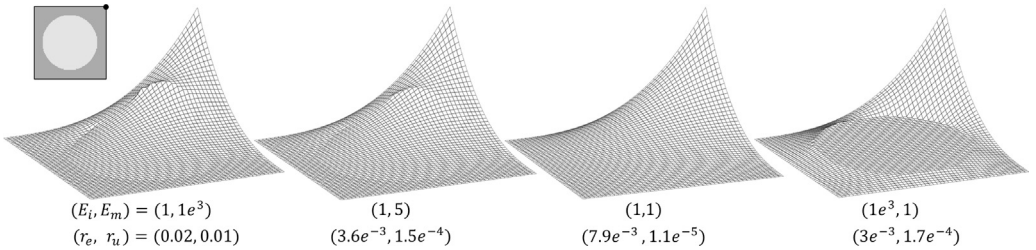

Fig. 16. Surfaces of the first shape function component $\mathbf{N}_{11}(\mathbf{x})$ and the effectivity indices for different material contrasts.

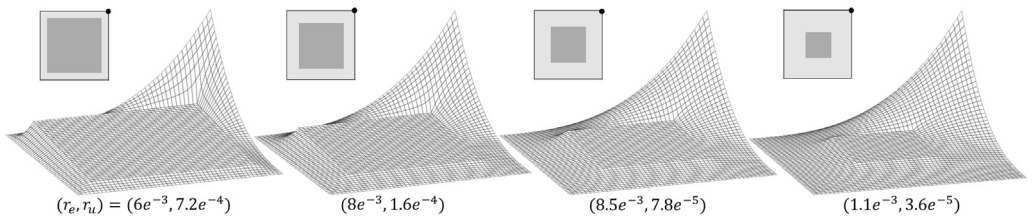

Fig. 17. Surfaces of the first shape function components $\mathbf{N}_{11}(\mathbf{x})$ and the effectivity indices for different-sized squared inclusions.

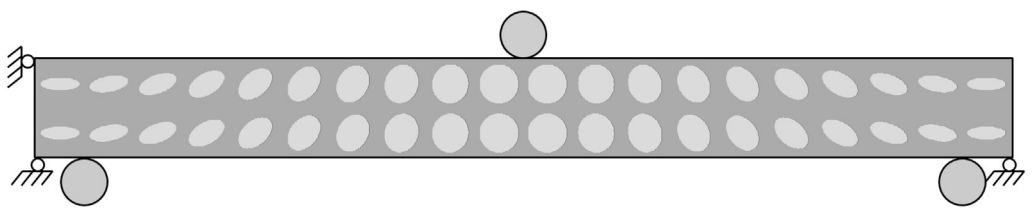

Fig. 18. Structure of a heterogeneous bending problem, where the body is imposed by loading fields in its vicinity described by Eq. (74), mimicking its contact forces with cylinders.

Shape functions at different material contrasts. Fig. 16 shows the plots of the surfaces of the first shape function component $\mathbf{N}_{11}(\mathbf{x})$ at different contrasts of Young's modulus $(1, 1e^3)$, $(1, 5)$, $(1, 1)$, and $(1e^3, 1)$ for inclusions and the matrices. As evident, the surface presents a smooth variation in the case of $(1, 1)$. In contrast, it drops rapidly over the softer inclusion in case (a) and remains almost unchanged over the stiffer inclusions in (d). Thus, the results demonstrate the proposed CBN shape functions' level of adaptation to the variations in the material stiffness.

Shape functions at different sizes of inclusions. Fig. 17 further shows the plots of the surfaces of the first component $\mathbf{N}_{11}(\mathbf{x})$ for the case of different-sized squared inclusions, where the darker and lighter regions have a Young's modulus of $E = 1e^3$ and $E = 1$, respectively. The surfaces of the shape functions clearly exhibit flatter variations right above the squared stiffer area, which is consistent with the expectation.

6.4. 2D heterogeneous bending beam

A more complex 2D heterogeneous bending beam example in Fig. 18 is also considered to test CBN's performance under different coarse mesh sizes. Compared with the MBB example in Fig. 12(a), the example is more challenging as it has a more complex design domain of larger size and more complex boundary conditions. In addition, the accuracy of its strain fields is analyzed in this example.

The bending beam is located at $(0, 0)$ in its bottom-left corner and has a size of 2×20. At three different locations (x_i^c, y_i^c) of coordinates of $(1, 0)$, $(10, 2)$, $(19, 0)$ from left to right, the body is imposed by a corresponding loading field in its vicinity, mimicking the contact forces with cylinders, which is described as

$$p(x) = p_i(1 - (x - x_i^c)^2). \tag{74}$$

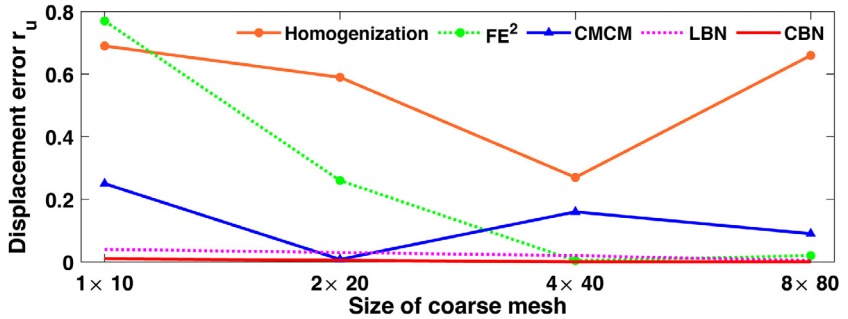

Fig. 19. Variations in effectivity indices r_u under different-sized coarse meshes: 1 × 10, 2 × 20, 4 × 40, and 8 × 80.

Table 5
Effectivity indices r_e, r_u at different-sized coarse meshes $\mathcal{M}^H$, compared with Homogenization, FE^2, CMCM, and CBN.

Size of $\mathcal{M}^H$	1 × 10 (r_e/r_u)	2 × 20	4 × 40 (cutting interfaces)	8 × 80 (cutting interfaces)
Homogenization	0.70/0.69	0.61/0.59	0.31/0.27	0.72/0.66
FE^2	1.00/0.77[a]	0.29/0.26	0.01/4e^{-3}	0.05/0.04
CMCM	0.23/0.25	0.01/8e^{-3}	0.11/0.16	0.09/0.09
CBN	0.02/0.01	6e^{-3}/5e^{-3}	1e^{-4}/6e^{-5}	5e^{-6}/2e^{-6}

[a]FE^2 fails to converge in this context.

where $p_1 = p_2 = 1$ and $p_3 = 2$. Further, the beam is fixed at the y-displacements on locations (0, 0) and (20, 0), and at the x-displacement on location (0, 2).

This example was modified from [21] with two main changes. First, it contains elliptic inclusions of varied shapes, instead of homogeneous circular inclusions of the same shape and size. Second, the inclusion is softer, whereas [21] has stiffer fibers; the former results in the tendency to produce a large deformation. In such a case, producing a highly accurate result is quite challenging.

The global fine mesh was set at a fixed size of 200 × 2000, and four coarse meshes of different sizes were set: 1 × 10, 2 × 20, 4 × 40, and 8 × 80. The effectivity indices r_u, r_e are summarized in Table 5, and variations of r_u are also plotted in Fig. 19. In general, the effectivity indices tend to decrease rapidly with increase in the coarse element number (producing a small-sized local mesh). This phenomenon can be explained based on two observations. First, the shape functions tend to capture finer material variations for a local fine mesh of a smaller size. Second, the global displacement tends to achieve a higher accuracy at the larger number of coarse DOFs.

However, three exceptions were also observed. First was Homogenization at 8 × 80, where the coarse mesh displayed a highly unordered distribution that strongly breaks the scale separation assumption. Second was FE^2 at 1 × 10, which may originate from the non-convergence of its nonlinear iteration. Third was CMCM at 4 × 40, where a high material contrast along the coarse boundary posed a more challenging analysis task [21]. However, the CBN addressed these situations well, and exhibited the smallest effectivity index of $r_e = 6e^{-3}$ and $r_u = 5e^{-3}$.

Fig. 20 shows the plots of the deformation and strain fields of the beam for a coarse mesh size of 2 × 20, compared with that of the benchmark. The computed results using the CBN were found to be remarkably close to the benchmark results, even in the middle large deformation area. Meanwhile, the overall deformation of CBN tended to be stiffer than the benchmark and certain local inconsistencies were observed, particularly across the coarse elements' interfaces. Similar phenomena were also observed in previous studies [21].

Comment. The above results were obtained using the same size of coarse mesh, wherein the CBN was observed to have more DOFs than the other approaches. For example, for a size 2 × 20, CBN had a DOF of 534 (depending on the number of CBNs) while all the other approaches had a DOF of 126 (depending on the corner node number). To further examine this, the performance of the other approaches was observed for the size of 8 × 80 with 1458 DOFs, which was approximately three times that of CBN (534). However, CBN still achieved approximately an order of accuracy improvement, specifically, $4e^{-3}$ (LBN), $2e^{-6}$ (CBN) in comparison with 0.66 (Homogenization),

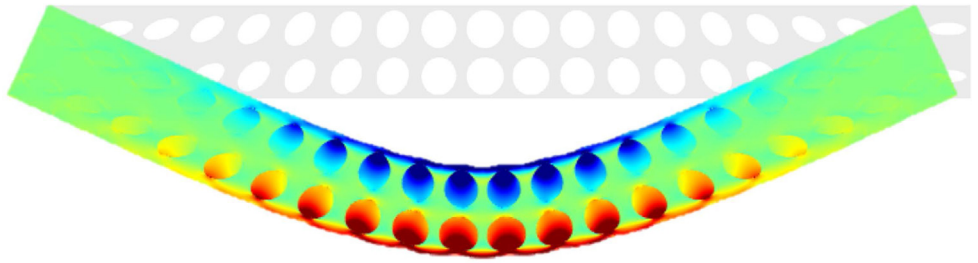

(a) Benchmark, ε_{11}

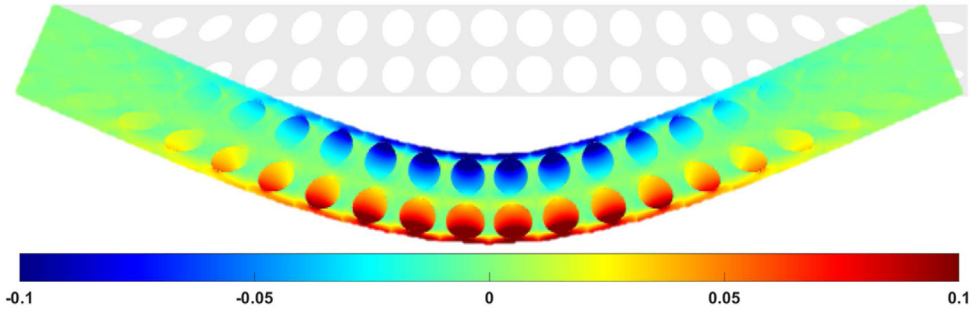

(b) CBN, ε_{11}

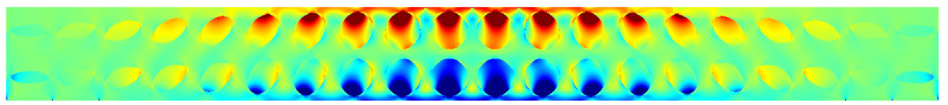

(c) Benchmark, ε_{22}

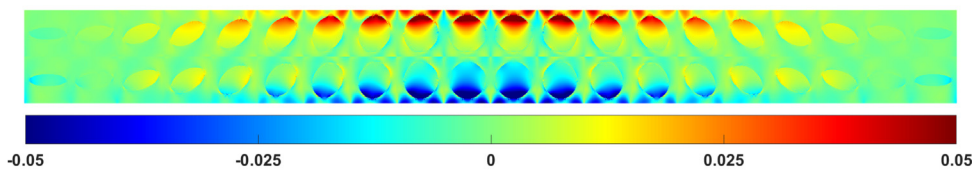

(d) CBN, ε_{22}

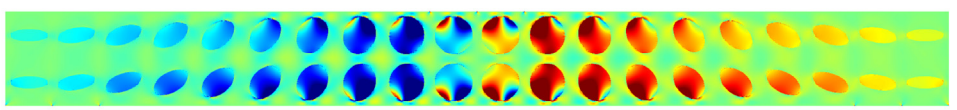

(e) Benchmark, ε_{12}

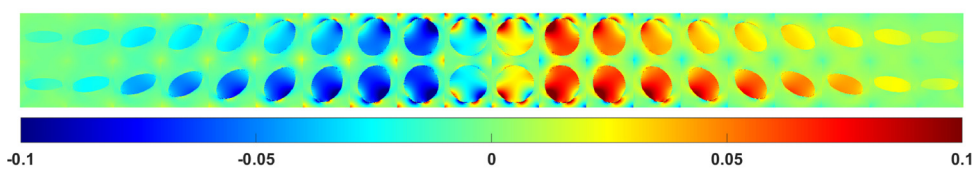

(f) CBN, ε_{12}

Fig. 20. Numerical results of CBN approach in comparison with the benchmarks, where the color bars are shown at the bottom of each subfigure. Note also the model presents an asymmetric deformation although their strains ε_{11} and ε_{22} are symmetric.

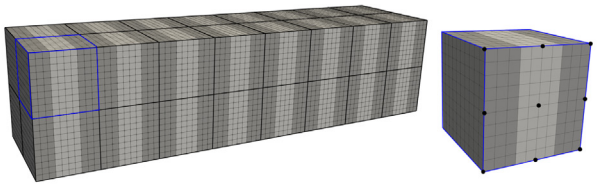

(a) Structure of $2 \times 2 \times 8$ coarse mesh, each containing a $10 \times 10 \times 10$ local fine mesh with 3×3 bridge nodes on one face

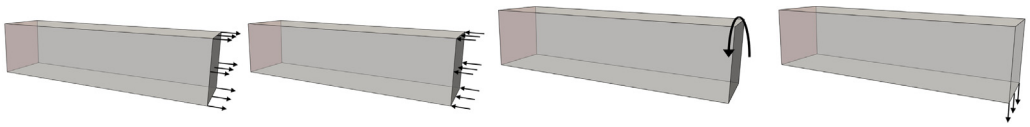

(b) Stretching (c) Compressing (d) Twisting (e) Bending

Fig. 21. A 3D example under four different loading conditions: stretching, compressing, twisting, and bending, where the red shadows denote the fixed area, and the black shadows and arrows denote the loading forces. (For interpretation of the references to color in this figure legend, the reader is referred to the web version of this article.)

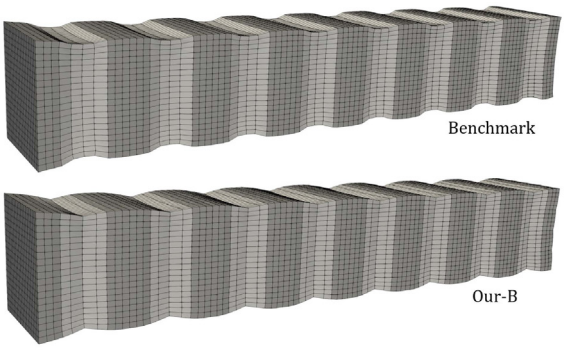

(a) Stretching, $r_e = 2.4e^{-4}, r_u = 8.9e^{-4}$

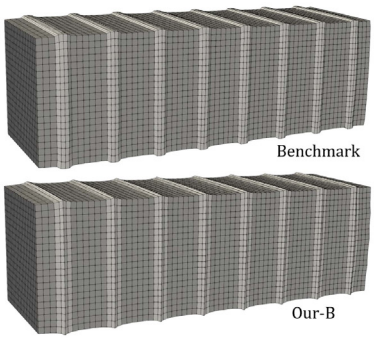

(b) Compressing, $r_e = 6.5e^{-4}, r_u = 8.9e^{-4}$

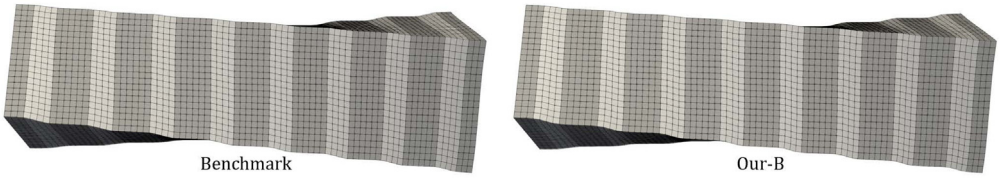

(c) Twisting, $r_e = 1.8e^{-4}, r_u = 3.1e^{-4}$

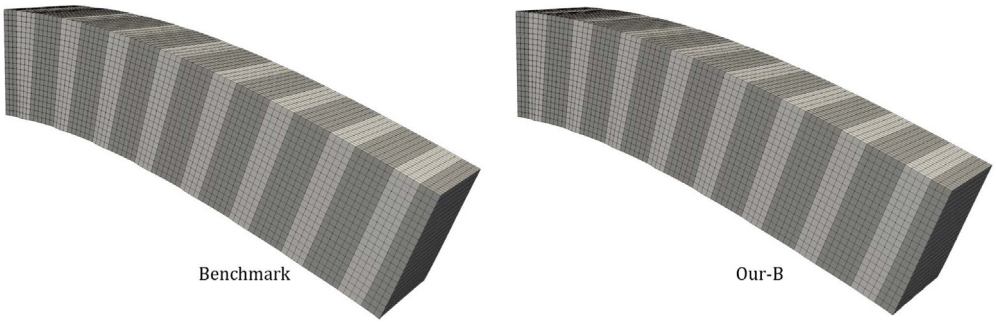

(d) Bending, $r_e = 1.4e^{-3}, r_u = 1.5e^{-3}$

Fig. 22. Numerical results and the effectivity indices for the 3D example in Fig. 21 compared with the benchmarks, where the benchmarks in (a),(b) are on the top and in (c),(d) are on the left.

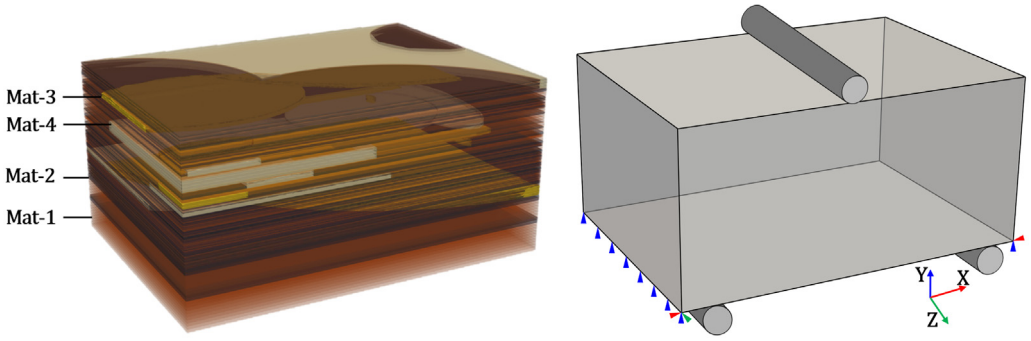

(a) Material distribution (b) A bending example

Fig. 23. Industrial 3D geologic model of 2.05 billion DOFs to test the performance of the proposed approach in heterogeneous structure analysis. The body is imposed by loading fields in its vicinity defined by Eq. (74), mimicking its contact forces with cylinders. (For interpretation of the references to color in this figure legend, the reader is referred to the web version of this article.)

Table 6
Mechanical properties of different soil layers in the geologic model in Fig. 23.

Index	Soil layer	Bulk modulus K	Shear modulus G
Mat-1 (brown)	Miscellaneous fill	$7e^6$	$3.2e^6$
Mat-2 (coffee)	Silty clay	$1.86e^7$	$9e^6$
Mat-3 (yellow)	Strong weathering rock	$1.38e^8$	$5.96e^7$
Mat-4 (buff)	Middle weathering rock	$6.3e^8$	$3.86e^8$

0.02 (FE^2), 0.09 (CMCM), as indicated in Fig. 19 for a coarse mesh of size 8×80. These observations indicate that CBN possesses an intrinsic flexibility in closely capturing the heterogeneity of the coarse element, which greatly improves its potential for the analysis of heterogeneous structures of non-separated scales. Moreover, its flexibility in choosing different DOFs further improves its potential.

6.5. Heterogeneous 3D example under different loading conditions

The performance of CBN under different loading conditions was tested on the 3D example in Fig. 21, where the dark and light areas have Young's modulus of $E = 1e^4$ and $1e^3$, respectively. The model had a coarse mesh size of $2 \times 2 \times 8$ and a local fine mesh size of $10 \times 10 \times 10$, with each coarse mesh face comprising a set of 3×3 coarse bridge nodes.

The example was tested under four classical loading cases: stretching, compressing, twisting, and bending, and the results are shown in Fig. 22 in comparison with the benchmark results. The largest effectivity index values obtained in the tests were $r_e = 1.4e^{-3}$ and $r_u = 1.5e^{-3}$, demonstrating the high approximation accuracy of the proposed approach. In this analysis, all the coarse elements had the same heterogeneity distribution. Thus, using CBN, the shape functions can be affordably computed offline once for a single coarse element, irrespective of the different loading conditions.

6.6. Practical 3D large-scale geologic model with 2.05 billion DOFs

A modified industrial 3D large-scale complex geologic model in Fig. 23(a) was analyzed using CBN. The model contained four types of materials in different colors: miscellaneous fill (brown), silty clay (coffee), strong weathering rock (yellow), and middle weathering rock (buff); the property parameters are listed in Table 6. It was fixed on its left and right sides, and exposed to three different pressure fields with $P = 1e^5$ induced by the contact cylinders at its top or bottom, as shown in Fig. 23(b).

In the analysis, the size of coarse mesh was $20 \times 30 \times 42$, whereas that of the local fine mesh was $30 \times 30 \times 30$, which combined to results in a global fine mesh size of $600 \times 900 \times 1260$, involving approximately 2.05 billion

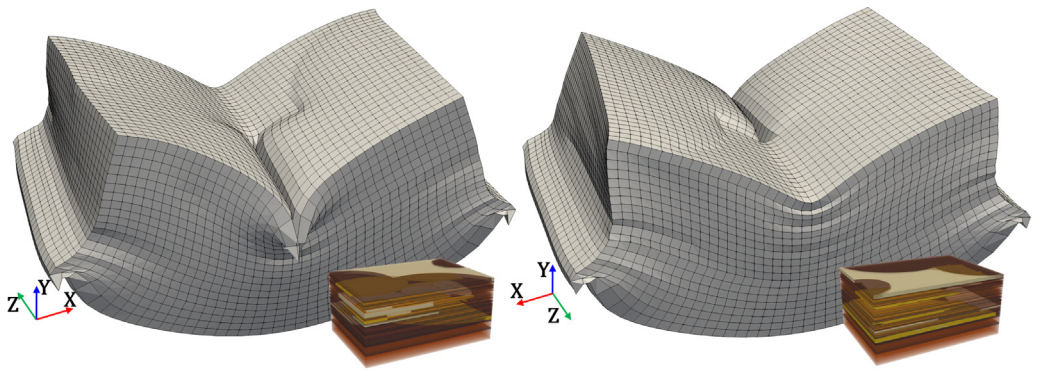

(a) Global deformation of $\mathcal{M}^H$ in different views

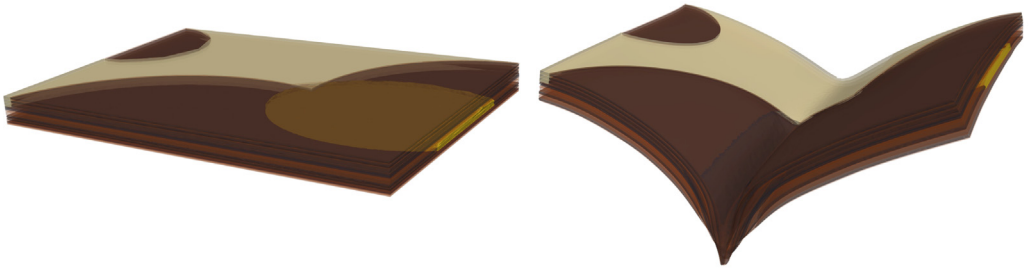

(b) Deformation of top layers in overall view

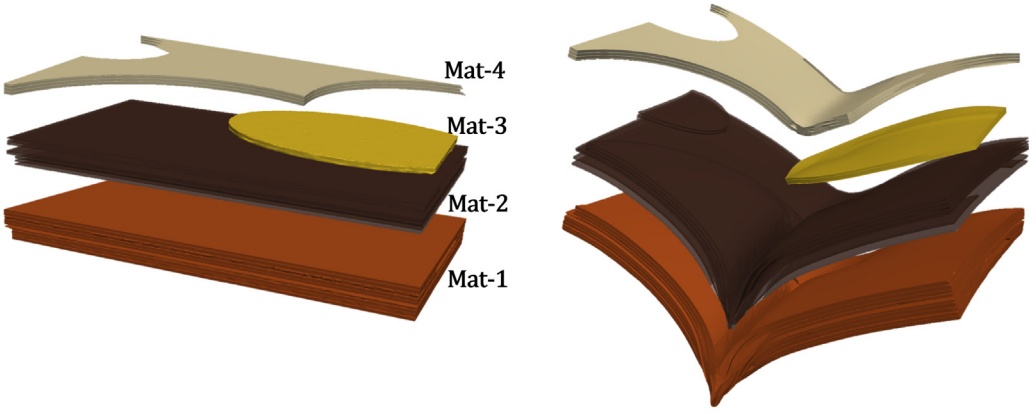

(c) Deformations of top layers in isolation

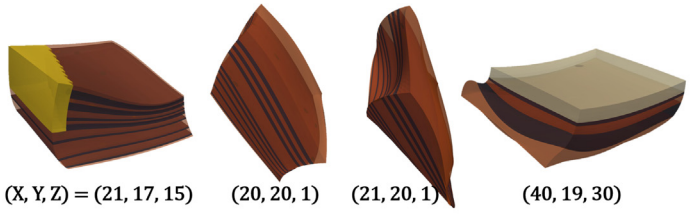

(d) Local deformation of four different $\mathcal{M}^{\alpha,h}$

Fig. 24. The numerical results on the geologic model in Fig. 23, where constructing the shape functions takes 6.6 s per coarse element, and computing the global deformation takes 1.2 h. (For interpretation of the references to color in this figure legend, the reader is referred to the web version of this article.)

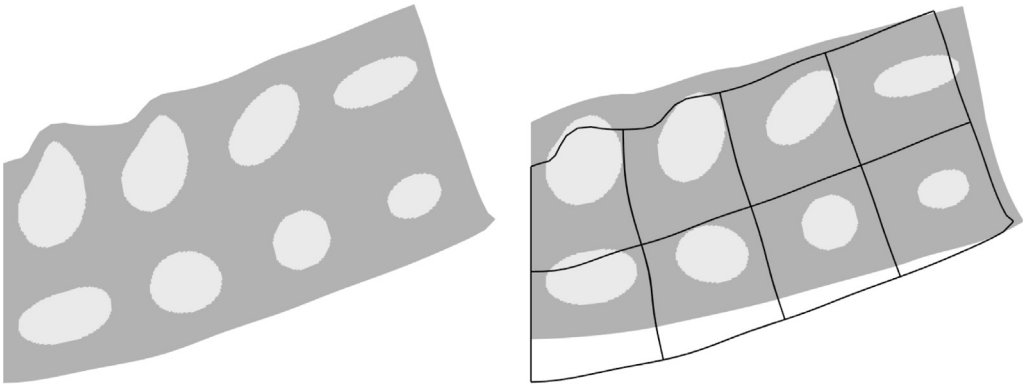

(a) Benchmark (b) Results of this study, $r_e = 2.5e^{-6}$, $r_u = 0.07$

Fig. 25. Numerical results for half MBB in Fig. 11 of nonlinear neo-Hookean material, where the black outlines in (b) denote the benchmark deformation. (For interpretation of the references to color in this figure legend, the reader is referred to the web version of this article.)

DOFs. Further, the corner nodes were set as the bridge nodes. This was an offline local analysis problem of 89-thousand DOFs, and an online global analysis problem of 1.5 million DOFs. The local computation required 6.6 s per coarse element, whereas the global computation required 1.2 h using the conjugate gradient (CG) method and ended with a relative residual $9.5e^{-7}$ in 8658 iterations.

Fig. 24 shows the plots of the overall deformations in (a), and the deformations of certain top layers (1/6 of the whole height) in (b) and (c). A close-up of the deformation in certain heterogeneous coarse elements is shown in (d). As evident, different deformation behaviors were observed in these different regions: the softer region demonstrated relatively large deformations (in brown and coffee) while the stiffer region exhibited small deformations (in buff and yellow). Such phenomena were also observed in different areas in a single coarse element, as shown in (d), thereby demonstrating the ability of the proposed approach in describing finely detailed local deformations of a heterogeneous structure.

The example yielded estimated effectivity indices r_e and r_u having values 0.09 and 0.08, respectively, computed as follows. The multitude of DOFs of the fine mesh and the unavailability of an HPC precluded to compute a benchmark result directly using the solution from the fine mesh. However, the accuracy of the CBN-based analysis approach was primarily dependent on the recover ability of the constructed CBN shape functions rather than the size of coarse mesh, and the former was further determined owing to the heterogeneities and size of the local fine mesh. Thus, based on the observation, a low-resolution geologic model of size $90 \times 120 \times 150$ (16.6 million DOFs) was regenerated based on the original one, and the local fine mesh size remained unchanged at $30 \times 30 \times 30$, resulting in a coarse mesh of size $3 \times 4 \times 5$.

6.7. Extension to nonlinear elastic model

Performance of the proposed CBN-based analysis approach for nonlinear elastic models was tested. Consider the half MBB in Fig. 11 of neo-Hookean materials at a loading of 10. All the other parameters remained unchanged similar to the setting in Section 6.1. The computed deformation was plotted as shown in Fig. 25, in comparison with the benchmark.

In contrast to the linear case, r_e and r_u exhibited very different values: $r_e = 2.5e^{-6}$ and $r_u = 0.07$. The small value of r_e indicates that global deformation energy was attained, which is the same as that of the benchmark. However, pseudo-stiffness was still present as indicated by the large quantity $r_u = 0.07$. This is believed to be caused by the local linear elasticity analysis in constructing the proposed CBN shape functions. Consequently, employing a nonlinear model to build more advanced shape function appears to be a reasonable choice for future research exploration.

7. Conclusions

This study introduced the concept of CBNs and their associated CBN shape functions to realize the elasticity analysis of heterogeneous structures of non-separated scales. The shape functions were derived per coarse element

as a product of the Bézier interpolation and boundary–interior transformations, which resulted in shape functions in the form of an explicit matrix representation.

The Bézier interpolation transformation ensured the displacement smoothness between adjacent coarse elements while providing additional variables to reduce the problem of inter-element stiffness. Whereas, the boundary–interior transformation, derived from the local stiffness matrix to the local fine mesh, offered a prominent advantage to finely embed the intrinsic material heterogeneity into the shape functions. Finally, the derived shape functions exhibited the properties of basic FE shape functions, thereby avoiding non-physical behavior. Extensive numerical examples indicated that the CBN has an intrinsic flexibility in closely capturing the heterogeneity of the coarse element, and it may serve as a suitable method for the analysis and optimization of heterogeneous structures without scale separation [29,36,45].

However, it was found that extensions of the CBN shape functions to nonlinear elasticity analysis problems may encounter accuracy loss. Thus, the introduction of nonlinear analysis in the shape function construction appears to be a very promising approach for the improvement of its analysis accuracy and warrants further research efforts. In addition, the shape functions can be computed in parallel, which boosts their applications in analysis of super-large problems, although their achievement still depends on the availability of appropriate computational facilities. Consequently, developing a surrogate model using techniques of model reduction [36,46] or deep learning [47,48] is expected to aid in resolving the existing limitations and thus should be explored in future studies.

Declaration of competing interest

The authors declare that they have no known competing financial interests or personal relationships that could have appeared to influence the work reported in this paper.

Acknowledgments

The study described in this paper is partially supported by the National Key Research and Development Program of China (No. 2018YFB1700603), the NSF of China (No. 61872320), and the Zhejiang Provincial Science and Technology Program in China (No. 2021C01108).

References

[1] A. Khademhosseini, R. Langer, A decade of progress in tissue engineering, Nat. Protoc. 11 (10) (2016) 1775–1781.
[2] P. Fratzl, R. Weinkamer, Nature's hierarchical materials, Prog. Mater. Sci. 52 (8) (2007) 1263–1334.
[3] K. Matouš, M.G. Geers, V.G. Kouznetsova, A. Gillman, A review of predictive nonlinear theories for multiscale modeling of heterogeneous materials, J. Comput. Phys. 330 (2017) 192–220.
[4] G.B. Olson, Computational design of hierarchically structured materials, Science 277 (5330) (1997) 1237–1242.
[5] J.H. Panchal, S.R. Kalidindi, D.L. McDowell, Key computational modeling issues in integrated computational materials engineering, Comput. Aided Des. 45 (1) (2013) 4–25.
[6] J. Alexandersen, B.S. Lazarov, Topology optimisation of manufacturable microstructural details without length scale separation using a spectral coarse basis preconditioner, Comput. Methods Appl. Mech. Eng. 290 (2015) 156–182.
[7] J. Yvonnet, When scales cannot be separated: Direct solving of heterogeneous structures with an advanced multiscale method, in: Computational Homogenization Of Heterogeneous Materials With Finite Elements, Springer, 2019, pp. 145–160.
[8] Y. Yu, H. Liu, K. Qian, H. Yang, M. McGehee, J. Gu, D. Luo, L. Yao, Y.J. Zhang, Material characterization and precise finite element analysis of fiber reinforced thermoplastic composites for 4D printing, Comput. Aided Des. 122 (2020) 102817.
[9] M. Raschi, O. Lloberas-Valls, A. Huespe, J. Oliver, High performance reduction technique for multiscale finite element modeling (HPR-FE^2): Towards industrial multiscale FE software, Comput. Methods Appl. Mech. Eng. 375 (2021) 113580.
[10] J. Teo, C. Chui, Z. Wang, S. Ong, C. Yan, S. Wang, H. Wong, S. Teoh, Heterogeneous meshing and biomechanical modeling of human spine, Med. Eng. Phys. 29 (2) (2007) 277–290.
[11] M. Nesme, P.G. Kry, L. Jeřábková, F. Faure, Preserving topology and elasticity for embedded deformable models, ACM Trans. Graphics (TOG) 28 (3) (2009) 52.
[12] J. Chen, H. Bao, T. Wang, M. Desbrun, J. Huang, Numerical coarsening using discontinuous shape functions, ACM Trans. Graphics (TOG) 37 (4) (2018) 1–12.
[13] C. Farhat, F.X. Roux, A method of finite element tearing and interconnecting and its parallel solution algorithm, Int. J. Numer. Methods Eng. 32 (6) (1991) 1205–1227.
[14] P.L. Tallec, Y. Roeck, M. Vidrascu, Domain decomposition methods for large linearly elliptic three dimensional problems, J. Comput. Appl. Math. 34 (1) (2006) 93–117.
[15] N. Spillane, An adaptive multipreconditioned conjugate gradient algorithm, SIAM J. Sci. Comput. 38 (3) (2016) A1896–A1918.
[16] W.L. Briggs, V.E. Henson, S.F. McCormick, A Multigrid Tutorial, Second ed., Society for Industrial and Applied Mathematics, 2000.

[17] K. Stüben, Algebraic multigrid (AMG): experiences and comparisons, Appl. Math. Comput. 13 (3–4) (1983) 419–451.
[18] K. Stüben, A review of algebraic multigrid, in: Numerical Analysis: Historical Developments In The 20th Century, Elsevier, 2001, pp. 331–359.
[19] A. Toselli, O.B. Widlund, Domain Decomposition Methods - Algorithms And Theory, Springer, 2005.
[20] D. Göddeke, Fast and accurate finite element multigrid solvers for PDE simulations on GPU clusters, 2010.
[21] M.V. Le, J. Yvonnet, N. Feld, F. Detrez, The coarse mesh condensation multiscale method for parallel computation of heterogeneous linear structures without scale separation, Comput. Methods Appl. Mech. Eng. 363 (2020) 112877.
[22] J. Pinho-da Cruz, J. Oliveira, F. Teixeira-Dias, Asymptotic homogenisation in linear elasticity. Part I: Mathematical formulation and finite element modelling, Comput. Mater. Sci. 45 (4) (2009) 1073–1080.
[23] P.W. Chung, K.K. Tamma, R.R. Namburu, Asymptotic expansion homogenization for heterogeneous media: computational issues and applications, Compos. Part A: Appl. Sci. Manuf. 32 (9) (2001) 1291–1301.
[24] E. Andreassen, C.S. Andreasen, How to determine composite material properties using numerical homogenization, Comput. Mater. Sci. 83 (2014) 488–495.
[25] O. Sigmund, Materials with prescribed constitutive parameters: an inverse homogenization problem, Int. J. Solids Struct. 31 (17) (1994) 2313–2329.
[26] L. Xia, P. Breitkopf, Design of materials using topology optimization and energy-based homogenization approach in MATLAB, Struct. Multidiscip. Optim. 52 (6) (2015) 1229–1241.
[27] R. Smit, W. Brekelmans, H. Meijer, Prediction of the mechanical behavior of nonlinear heterogeneous systems by multi-level finite element modeling, Comput. Methods Appl. Mech. Eng. 155 (1–2) (1998) 181–192.
[28] F. Feyel, A multilevel finite element method (FE^2) to describe the response of highly non-linear structures using generalized continua, Comput. Methods Appl. Mech. Eng. 192 (28–30) (2003) 3233–3244.
[29] L. Xia, P. Breitkopf, Concurrent topology optimization design of material and structure within FE^2 nonlinear multiscale analysis framework, Comput. Methods Appl. Mech. Eng. 278 (2014) 524–542.
[30] V. Kouznetsova, M. Geers, W. Brekelmans, Multi-scale constitutive modelling of heterogeneous materials with a gradient-enhanced computational homogenization scheme, Int. J. Numer. Methods Eng. 54 (8) (2002) 1235–1260.
[31] V. Kouznetsova, M.G. Geers, W. Brekelmans, Multi-scale second-order computational homogenization of multi-phase materials: a nested finite element solution strategy, Comput. Methods Appl. Mech. Eng. 193 (48–51) (2004) 5525–5550.
[32] J. Yvonnet, Computational Homogenization Of Heterogeneous Materials With Finite Elements, Springer, Cham, 2019.
[33] A. Tognevi, M. Guerich, J. Yvonnet, A multi-scale modeling method for heterogeneous structures without scale separation using a filter-based homogenization scheme, Int. J. Numer. Methods Eng. 108 (1) (2016) 3–25.
[34] V.B.C. Tan, K. Raju, H.P. Lee, Direct FE^2 for concurrent multilevel modelling of heterogeneous structures, Comput. Methods Appl. Mech. Eng. 360 (2020) 112694.
[35] J. Schröder, A numerical two-scale homogenization scheme: the FE^2-method, in: Plasticity And Beyond: Microstructures, Crystal-Plasticity And Phase Transitions, Springer Vienna, Vienna, 2014, pp. 1–64.
[36] Z. Wu, L. Xia, S. Wang, T. Shi, Topology optimization of hierarchical lattice structures with substructuring, Comput. Methods Appl. Mech. Eng. 345 (2019) 602–617.
[37] Z. Liu, L. Xia, Q. Xia, T. Shi, Data-driven design approach to hierarchical hybrid structures with multiple lattice configurations, Struct. Multidiscip. Optim. (2020) 1–9.
[38] T.Y. Hou, X.-H. Wu, A multiscale finite element method for elliptic problems in composite materials and porous media, J. Comput. Phys. 134 (1) (1997) 169–189.
[39] Y. Efendiev, J. Galvis, X.-H. Wu, Multiscale finite element methods for high-contrast problems using local spectral basis functions, J. Comput. Phys. 230 (4) (2011) 937–955.
[40] G. Farin, Curves And Surfaces For CAGD (Fifth Edition) A Practical Guide, Morgan Kaufmann, 2001.
[41] O.C. Zienkiewicz, R.L. Taylor, The Finite Element Method: Its Basis and Fundamentals, Butterworth-Heinemann, 2013.
[42] J.M. Melenk, I. Babuška, The partition of unity finite element method: basic theory and applications, Comput. Methods Appl. Mech. Eng. 139 (1–4) (1996) 289–314.
[43] S. Rajendran, B. Zhang, A "FE-meshfree" QUAD4 element based on partition of unity, Comput. Methods Appl. Mech. Eng. 197 (1–4) (2007) 128–147.
[44] A.F. Bower, Applied Mechanics Of Solids, CRC Press, 2009.
[45] J. Gao, Z. Luo, H. Li, L. Gao, Topology optimization for multiscale design of porous composites with multi-domain microstructures, Comput. Methods Appl. Mech. Eng. 344 (2019) 451–476.
[46] F. El Halabi, D. González, A. Chico, M. Doblaré, FE^2 multiscale in linear elasticity based on parametrized microscale models using proper generalized decomposition, Comput. Methods Appl. Mech. Eng. 257 (2013) 183–202.
[47] K. Bhattacharya, B. Hosseini, N.B. Kovachki, A.M. Stuart, Model reduction and neural networks for parametric PDEs, SIAM J. Comput. Math. 7 (2021) 121–157.
[48] K.O. Lye, S. Mishra, D. Ray, P. Chandrashekar, Iterative surrogate model optimization (ISMO): An active learning algorithm for PDE constrained optimization with deep neural networks, Comput. Methods Appl. Mech. Eng. 374 (2021) 113575.